A nonlinear analytical formulation for the 1D modelling of a flexible beam in channel flow

Filipe Soares, Jose Antunes, Vincent Debut, Christophe Vergez, Bruno Cochelin, Fabrice Silva

A nonlinear analytical formulation for the 1D modelling of a flexible beam in channel flow

Filipe Soares[1]*, Jose Antunes[1], Vincent Debut[2], Christophe Vergez[3], Bruno Cochelin[3], Fabrice Silva[3]

[1] Instituto Superior Técnico – Centro de Ciências e Tecnologias Nucleares, Lisboa, Portugal
{filipe.soares@ctn.tecnico.ulisboa.pt, jantunes@ctn.tecnico.ulisboa.pt}

[2] Instituto Politécnico de Castelo Branco – Escola de Artes Aplicadas, Castelo Branco, Portugal
{vincentdebut@ipcb.pt}

[3] Aix-Marseille Université, CRNS, Centrale Marseille, LMA UMR7031, Marseille, France
{vergez@lma.cnrs-mrs.fr, bruno.cochelin@centrale-marseille.fr, silva@lma.cnrs-mrs.fr}

*Corresponding author

Keywords: Flow-induced vibration, nonlinear analytical modeling, beam in axial flow, impact modelling

Abstract

The dynamics of flexible beams in confined flows has been a subject of research for many years, as its fundamental behaviour is found in many applications, from energy harvesters to musical instruments. Most studies are concerned solely with the conditions for linear stability and do not explore the ensuing nonlinear behaviour of the system. This is particularly delicate as fluttering beams in confined flows are known to often result in dynamics with intermittent impacts between the beam and the side-walls. Here we present a nonlinear analytical resolution to a simplified 1-D model, based on a modal beam and bulk-flow equations. The model accounts for dissipation through distributed frictional and localised head-loss terms. The latter are imposed at the boundary conditions and aims to describe the complex effects occurring outside the domain (turbulence, vortex shedding, etc.). The present analytical resolution leads to a compact system for linear stability analysis, but also to a nonlinear formulation of the fluid-structure interaction. The inclusion of a regularized contact model allows for the computation of the full nonlinear dynamics, including intermittent impacts. Linear stability results are compared to previously published results using 2-D CFD models, and the relative merits of the model are discussed. A variety of limit cycles, (1) with and without impacts, (2) in symmetric and asymmetric configurations and (3) with impacts both at the beam tip and along its length, are shown to illustrate the diversity of dynamics encountered. Moreover, we show that, at large flow velocities, particular model configurations can lead to aperiodic dynamics, a phenomenon reported in several experimental observations. To the authors knowledge, the proposed formulation presents, for the first time, a framework for the comprehensive understanding of the nonlinear dynamics associated with flexible beams in confined axial flow.

1 Introduction

The static and dynamic instabilities associated with flexible plates subject to axial flow occur in a variety of contexts from enhanced heat transfer [1] [2], energy harvesting devices [3] [4], wind musical instruments [5] [6] or palatal snoring [7] [8]. The subject has been studied extensively [9] [10], particularly for the case of unconfined flows.

Flexible beams in axial flow present a wide variety of dynamical behaviour. The work of Kornecki et al. [11] and Guo & Paidoussis [12] explored the critical flow velocities for plates with various boundary conditions and the associated type of instabilities emerging. They studied analytical solutions of 2D models, based on inviscid incompressible flow, where instability is caused by perturbation pressures stemming from the linearized unsteady Bernoulli equation at the fluid-beam boundary. Results show that plates can lose stability by divergence, single-mode flutter or coupled-mode flutter, depending on the support conditions at the leading and trailing edges. In summary, their results suggested that plates fixed at both ends first lose stability by divergence but can also undergo post-divergent flutter, while plates with one free-end typically lose stability either by single-mode or coupled-mode flutter, depending on particular flow-beam configurations.

This work will focus on the particular case of cantilever plates/beams in axial flow, a widely studied canonical example of flow-induced vibrations [7] [8] [13] [14]. In these systems, the typical instability is of the flutter type. In the work of Shoele & Mittal [2], we find some elucidating results regarding the influence of relevant non-dimensional parameters like the fluid-beam mass ratio or the confinement ratio (channel height to beam length ratio). Their results show that, at low beam-fluid mass ratios, the instability is of the single-mode flutter type, involving the coupling of the first two in-vacuo beam modes. As mass ratios increase, the initial single-mode flutter ceases to be the principal instability, and successive "mode-transitions" occur, whereby multiple higher-order fluttering modes prevail. This type of instability is commonly referred to as coupled-mode flutter. Additionally, the effect of confinement is reported to have a destabilizing effect, leading to lower critical velocities as well as the emergence "mode-transitions" at lower mass ratios.

More recently, the advances in computational efficiency have enabled the possibility to simulate these fluid-structure interaction (FSI) systems numerically by solving the Navier-Stokes equations in 2D and 3D domains [2] [15]. These FSI models allow a more accurate representation of the physics and provide a useful validation tool for simpler analytical models, indicating under which conditions they are able to describe more complex 2D/3D phenomena [16]. However useful, Computational Fluid Dynamics (CFD) models require considerable computational time, which becomes a handicap when analysing problems whose behaviour depends on a wide variety of parameters. Nevertheless, we emphasize the work of Cisonni et al. [17] that, despite considerable computational effort (reported 150,000 CPU hours), managed to present a wide set of reference solutions describing the variation of stability boundaries in terms of the most pertinent non-dimensional parameters: the reduced velocity, mass ratio, confinement ratio and Reynolds number. However, for a more thorough parameter mapping, 1D models, based on simplified equations of motion, are not only computationally more efficient but also more tractable, and may provide valuable insights into the core dynamics of the problem.

In the context of simplified approaches, we note the work of Nagakura & Kaneko [18] that have used leakage flow theory to model the linear stability of a cantilever beam in a confined passage. Based on the work by Inada & Hayama [19] [20], they formulate a 1D problem where flow pressure and velocity are taken as cross-sectionally averaged. The confinement is restricted to symmetric channels of constant cross-section, viscous effects are accounted for by a distributed friction term and the energy losses at the trailing edge are encapsulated by a localised head-loss term, imposed at the boundary condition. Moreover, Tosi & Colonius [16] have positively validated the stability results from a similar simplified model to those of direct numerical simulations using the Navier-Stokes equations in a 2D domain. They underline the potential of such modelling approaches as stability results converge over a wide range of fluid-beam mass ratios and Reynolds numbers, at least for relatively narrow passages. As the confinement ratio (channel height to beam length) increases, larger discrepancies are seen.

By and large, the analytical models developed so far deal solely with the conditions for instability, using linearized equations of motions to study the effect of various parameters on the stability boundaries.

Although undeniably a crucial information about the system dynamics, this gives us little insight about the ensuing nonlinear behaviour. The analysis of the nonlinear dynamics might by of valuable interest to various applications, giving information about the working regimes in wind musical instruments, human snoring or in energy harvesting devices.

In the context of unbounded flows, a number of theoretical and experimental studies can be found, illustrating the array of possible limit cycles arising in this type of systems [21] [22] [23] [24]. However, for instabilities in a confined passage, nonlinear modelling results and experimental observations have demonstrated the regular occurrence of limit cycles with intermittent impacts between the beam and the side walls [24] [25] [26] [27]. Hence, the nonlinear modelling becomes a non-trivial task as both the flow and the wall-structure contact phenomena need to be accounted for. Nonlinear dynamic studies can be found, for example, in the work of Wu and Kaneko [25] using a 1D model as well as in the work of Alben [24] using a CFD inviscid 2D model. However, both are constrained by the occurrence of impacts, allowing results only in a limited region of the parameter space.

In this paper, we deal with a simplified 1D model in the spirit of Nagakura & Kaneko's work [18]. Yet, the formal approach to solve the fluid-structure equations is distinct from those developed in [18]. Contrary to their work, we admit channel profiles of any shape. More importantly however, we present an analytical resolution, based on formal solutions of the flow pressure and velocity fields, that leads not only to a compact system for linear stability analysis but also to a fully nonlinear flow formulation. This formulation can be used to explore post-instability regimes at very low computational costs. Additionally, to overcome the previously mentioned limitations, we add the possibility of contact between the flexible beam and the channel walls and illustrate the wide diversity of dynamics encountered, including limit cycles with and without intermittent impacts as well as the possibility of aperiodic/chaotic behaviour.

2 Model description

The model presented here deals with the fluid-structure interaction of a flexible beam confined by flow on each upper and lower sides, as illustrated in Figure 1. The formulation presented in the following is generic, in that it can, in principle, be applied to beams with arbitrary boundary conditions. However, for illustrative simplicity, in this paper we will deal solely with the particular case of a cantilever beam.

The flow in each channel is described by bulk-flow equations, where the pressure and velocity fields are taken as cross-sectionally averaged. We include distributed dissipation in the form of a Fanning friction term to describe boundary-layer/viscous effects. Moreover, localized dissipation at the entrance and exit of the domain is added in the form of local head-losses (or pressure losses). The latter are imposed at the boundary conditions using a classical quasi-static Bernoulli condition.

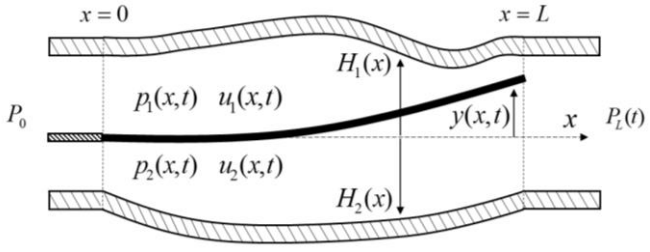

Figure 1 – Schematic description of the 1D model.

2.1 Structural dynamics

The dynamics of a flexible linear beam are defined in terms of N modes, decoupled from the fluid. The modal parameters: modal masses m_n, frequencies ω_n, damping ratios ζ_n and mode shapes $\phi_n(x)$ can be calculated analytically for a beam with uniform cross-section or numerically for beams of any geometry, through either the Euler-Bernoulli or Timoshenko 1D linear beam equations. As an example, using Euler-Bernoulli 1-D beam theory, a cantilevered beam with uniform cross-section will have frequencies defined by

$$\omega_n = \alpha_n^2 \sqrt{\frac{EI}{mL^4}} \tag{1}$$

where EI is the bending stiffness, m is the total mass of the beam, L is the beam length and α_n are the solutions of the characteristic equation

$$\cos(\alpha_n)\cosh(\alpha_n)+1=0 \tag{2}$$

while the modal masses will be $m_n = m/4$, for all modes. For simplicity we consider here a uniform beam with length L, width b and thickness e. The beam displacement is developed as

$$y(x,t) = \sum_{n=1}^{N} \phi_n(x) q_n(t) \tag{3}$$

and the beam motion is finally described by the following set of N modal equations

$$m_n \ddot{q}_n(t) + 2m_n \omega_n \zeta_n \dot{q}_n(t) + m_n \omega_n^2 q_n(t) = F_n(t) \quad , \quad n = 1,\, 2 \ldots N \tag{4}$$

where the modal forces $F_n(t)$ are given by the projection of the pressure fields $p_1(x,t)$ and $p_2(x,t)$, (associated with the flow in the upper and lower channels, respectively), unto the beam modes,

$$F_n(t) = b\int_0^L \Delta P(x,t)\phi_n(x)dx \quad , \quad n = 1,\, 2 \ldots N \tag{5}$$

where the pressure difference between the two channels is $\Delta P(x,t) = p_2(x,t) - p_1(x,t)$. As usual, the second-order system can also be described by a set of $2N$ first-order ODEs in terms of the modal displacements $q_n(t)$ and velocities $r_n(t) = \dot{q}_n(t)$

$$\begin{cases} \dot{q}_n(t) = r_n(t) \\ \dot{r}_n(t) + 2\omega_n \zeta_n r_n(t) + \omega_n^2 q_n(t) = F_n(t)/m_n \end{cases} \quad , \quad n = 1,\, 2 \ldots N \tag{6}$$

It should be noted that, for simplicity, we have neglected the effect of geometric nonlinearities of the beam. Including these nonlinear terms, although inconsequential for a linear stability analysis, could be important for the estimation of large amplitude beam oscillations. However, as will be discussed in the following section 2.2, the bulk-flow model used here assumes relatively narrow flow confinements. Contrary to systems dealing with unconfined flow, beam motion in these configurations is restricted by contact with the walls of a narrow channel, and it is therefore less likely that nonlinear geometric effects will be paramount, as is the case in unbounded configurations. Nevertheless, including terms describing geometric nonlinearities could be incorporated in the model in a straight forward manner, as done in [28] for example, in a modal framework.

2.2 Fluid dynamics

To derive the incompressible bulk-flow equations, we consider small-to-moderate fluctuating channel heights $h_c(x,t)$, defined in terms of the beam motion

$$\begin{cases} h_1(x,t) = H_1(x) - y(x,t) \\ h_2(x,t) = H_2(x) + y(x,t) \end{cases} \tag{7}$$

where $H_1(x)$ and $H_2(x)$ are the distances from each wall to the position of the beam at rest and the index $c = 1,2$ corresponds to the upper and lower channels, respectively. Because we assume the channel heights are small compared to the beam dimension L, the changes in fluid pressure $p_c(x,y,t)$ and velocity $u_c(x,y,t)$ along its cross-section are considered negligible. Then, the flow variables are taken as cross-

sectionally averaged, $p_c(x,t)$ and $u_c(x,t)$. Derivation of the 1D bulk-flow equations under these assumptions can be found in [29] for incompressible fluids, as will be assumed here. The continuity and momentum equations of the fluid are given, respectively, for each channel $c = 1, 2$, by

$$\frac{\partial h_c}{\partial t} + \frac{\partial}{\partial x}\left(h_c u_c\right) = 0 \tag{8}$$

$$\rho\left[\frac{\partial}{\partial t}\left(h_c u_c\right) + \frac{\partial}{\partial x}\left(h_c u_c^2\right)\right] + h_c \frac{\partial p_c}{\partial x} + \tau_c^w + \tau_c^b = 0 \tag{9}$$

where ρ is the fluid's density, τ_c^w and τ_c^b are the shear stresses at the two interfaces (fluid-wall and fluid-beam) in each channel. Following the bulk-flow approach, the tangential stresses will be formulated as a head-loss model, given by

$$\tau_c^{w,b} = \frac{1}{2}\rho u_c \mid u_c \mid f_c^{w,b} \tag{10}$$

where f_c^w and f_c^b are the Fanning friction coefficients for each interface. To maintain a generic formulation, we keep the modular term $u_c \mid u_c \mid$, instead of its quadratic simplification. This allows for flow in both directions, as well as locally reverse flow, which may occur at large amplitude beam motions. Additionally, we assume both interfaces have equivalent frictional properties, hence $f_c^w = f_c^b = f$.

It is well known that the Fanning friction coefficient f depends on the Reynolds number Re. The literature on this topic is vast and several models have been developed to approximate experimental observations [30] [31] [32]. The simplest, and most commonly used models, start from the assumption that f has a dependency relation to the Reynolds number, different in laminar and turbulent flows. Typical values of f for smooth surfaces are: $0.001 < f < 0.01$ for turbulent flows, and $0.01 < f < 1$ for laminar flows [31]. Some models combine the two relations (laminar and turbulent) to describe the friction factor in the full range of flows, including mixed laminar-turbulent flows (see, for example, the interesting discussion and formulation in [33]). These formulations might be of interest to include in the future as they eliminate incertitude and guesswork concerning this parameter, however, at the cost of slightly increasing model complexity. With that said, for the sake of simplicity we take f to be constant, which might be more reliable in turbulent ranges, where experiments show lower or even negligible dependency [31].

Aside from the distributed losses, we include as well singular dissipative effects at the boundaries. These are enforced at the boundary conditions and aim to encapsulate, in a simplified manner, the energy losses occurring outside the domain. The complex phenomena associated with these energy losses is diverse and can vary significantly with local geometry (e.g. area constriction/expansion) and flow conditions. However, a simple and common approach is to use a quasi-steady Bernoulli relation which includes head-loss terms, whose coefficients are typically taken from empirical data. This method is commonly used to treat leakage-flow instabilities [18] [19] [20]. Here, the boundary conditions are set as if two reference pressure chambers (where flow velocity is zero) exist far from the boundaries of the domain. Then, the localized head-loss terms will represent energy losses occurring in the path between the reference chambers and the domain entrance/exit. The second order system (8)-(9) is then submitted to the following flow boundary conditions at $x = 0$ and $x = L$:

$$p_c(0,t) = P_0(t) - \rho\frac{1}{2}u_c^2(0,t) - \rho\frac{1}{2}u_c(0,t)\left|u_c(0,t)\right|K_0 \tag{11}$$

$$p_c(L,t) = P_L(t) - \rho\frac{1}{2}u_c^2(L,t) + \rho\frac{1}{2}u_c(L,t)\left|u_c(L,t)\right|K_L \tag{12}$$

where K_0 and K_L are the singular head-loss coefficients at the boundaries; $P_0(t)$ and $P_L(t)$ are the imposed pressures at each reference chambers. For the particular case of a cantilevered beam, the head-loss coefficient K_0 is bound to have a minimal effect on the dynamics, as it acts on the clamped end of the beam. For steady inflow (in the positive $x-$direction), it acts simply as a control-valve, limiting the flow

energy entering the domain. On the other hand, the turbulent effects expected at the trailing-edge suggest that K_L will probably have a significant effect on the coupling dynamics. As a note, Kaneko et al. [34] have developed a model using similar head-loss coefficients. In these models, the authors assume values equivalent to $K_L = 1$ and $K_0 = 0$. Even though they only explored symmetric configurations, it is worth noting that experimental results correlated well with the predicted critical points. Moreover, Tosi and Colonius [16], compared the linear stability results stemming from a similar 1D model to simulations of a nonlinear 2D model. They showed that, with $K_0 = 0$ and $K_L = 1$, flutter boundaries are remarkably well predicted, provided the channel heights remain reasonably small compared to the beam length ($H/L > 1/10$, for channels with constant height).

3 Nonlinear analytical approach using formal solutions

The analytical resolution presented here is inspired by the work of Antunes & Piteau [29] [35]. In their work, analytical expressions for the fluid forces between two parallel plates are derived, leading to a single mode nonlinear lumped-parameter formulation, describing the interaction dynamics of a discrete oscillator subject to axial flow, including both distributed and singular head-losses. Here, we developed on the same idea, and apply it to the coupling of axial flow to a continuous flexible structure.

Integrating the continuity equation (8) with respect to x leads us to a formal solution for the velocity fields in each channel c:

$$u_c(x,t) = \frac{Q_c(t) - \int \dot{h}_c(x,t)dx}{h_c(x,t)} \tag{13}$$

where the "constants" of integration (actually, time domain functions) $Q_c(t)$ represent the global unsteady flow rates (per unit width) in each channel. After replacement of (13) in the momentum equation (9) and again integrating with respect to x, we obtain the formal solution for the pressure field in each channel,

$$p_c(x,t) = \rho \int \left(\begin{array}{c} \dfrac{\int \ddot{h}_c dx}{h_c} - 2\dfrac{\dot{h}_c \int \dot{h}_c dx}{h_c^2} + \dfrac{h_c' \left(\int \dot{h}_c dx \right)^2}{h_c^3} - \dfrac{1}{h_c}\dot{Q}_c(t) + 2\left(\dfrac{\dot{h}_c}{h_c^2} - \dfrac{h_c' \int \dot{h}_c dx}{h_c^3} \right) Q_c(t) \\ + \dfrac{h_c'}{h_c^3} Q_c(t)^2 + f\left(\dfrac{\left(\int \dot{h}_c dx - Q_c(t) \right) \left| \int \dot{h}_c dx - Q_c(t) \right|}{h_c^3} \right) \end{array} \right) dx + S_c(t) \tag{14}$$

where spatial and temporal derivatives are denoted by an upper dash and dot, respectively. The new "constants" of integration $S_c(t)$ describe the pressure at the entrance of the channels $S_c(t) = p_c(0,t)$, i.e. the pressure after the effect of the localised head-losses at $x = 0$. Note that the integral terms in (13) and (14) correspond to primitives (indefinite integrals) as their constants of integration are combinedly encapsulated in $Q_c(t)$ and $S_c(t)$.

From here on, to simplify notation, we define the following auxiliary variables describing the terms in the formal solutions

$$
\begin{aligned}
&A_c(x,t) = -\frac{\int \dot{h}_c dx}{h_c} \quad ; \qquad\qquad B_c(x,t) = \frac{1}{h_c} \quad ; \\
&C_c(x,t) = \frac{\int \ddot{h}_c dx}{h_c} - 2\frac{\dot{h}_c \int \dot{h}_c dx}{h_c^2} + \frac{\left(\int \dot{h}_c dx\right)^2}{h_c^3}\left(h_c^{'} + f\,\mathrm{sign}\left(\int \dot{h}_c dx - Q_c(t)\right)\right) ; \\
&D_c(x,t) = 2\left(\frac{\dot{h}_c}{h_c^2} - \frac{\int \dot{h}_c dx}{h_c^3}\left(h_c^{'} + f\,\mathrm{sign}\left(\int \dot{h}_c dx - Q_c(t)\right)\right)\right) ; \\
&E_c(x,t) = \frac{1}{h_c^3}\left(h_c^{'} + f\,\mathrm{sign}\left(\int \dot{h}_c dx - Q_c(t)\right)\right) ;
\end{aligned}
\tag{15}
$$

To enforce the boundary conditions, we replace the formal solutions (13)-(14) into expressions (11)-(12). After some algebra, we obtain two expressions for the constant of integration $S_c(t)$, in terms of $Q_c(t)$, $\dot{Q}_c(t)$ and the beam motion $A_c(x,t) - E_c(x,t)$. At the leading edge ($x = 0$) we have simply

$$
S_c(t) = P_0 - \rho\frac{1}{2}\left(1+\mathrm{sign}\left(Q_c(t)\right)K_0\right)\left(B_c(0,t)Q_c(t)\right)^2 \tag{16}
$$

while at the trailing edge ($x = L$) we get

$$
S_c(t) = P_L(t) - \rho\begin{pmatrix}
-\left(\int B_c(L,t)dx\right)\dot{Q}_c(t) \\
+\left(\int D_c(L,t)dx + A_c(L,t)B_c(L,t)\left[1-\mathrm{sign}\left(A_c(L,t)+B_c(L,t)Q_c(t)\right)K_L\right]\right)Q_c(t) \\
+\left(\int E_c(L,t)dx + \frac{B_c^2(L,t)}{2}\left[1-\mathrm{sign}\left(A_c(L,t)+B_c(L,t)Q_c(t)\right)K_L\right]\right)Q_c^2(t) \\
+\frac{A_c^2(L,t)}{2}\left[1-\mathrm{sign}\left(A_c(L,t)+B_c(L,t)Q_c(t)\right)K_L\right] + \int C_c(L,t)dx
\end{pmatrix}
\tag{17}
$$

Then, combining (17) and (16), we are able to remove the constant of integration $S_c(t)$ and obtain two (one for each channel) first-order nonlinear ODEs in terms of the unsteady flow rates $Q_c(t)$,

$$
\begin{aligned}
&-\left(\int B_c(L,t)dx\right)\dot{Q}_c(t) \\
&+\left(\int D_c(L,t)dx + A_c(L,t)B_c(L,t)\left[1-\mathrm{sign}\left(A_c(L,t)+B_c(L,t)Q_c(t)\right)K_L\right]\right)Q_c(t) \\
&+\left(\begin{array}{l}\int E_c(L,t)dx - \frac{B_c^2(0,t)}{2}\left(1+\mathrm{sign}\left(Q_c(t)\right)K_0\right) \\ +\frac{B_c^2(L,t)}{2}\left[1-\mathrm{sign}\left(A_c(L,t)+B_c(L,t)Q_c(t)\right)K_L\right]\end{array}\right)Q_c^2(t) \\
&+\frac{A_c^2(L,t)}{2}\left[1-\mathrm{sign}\left(A_c(L,t)+B_c(L,t)Q_c(t)\right)K_L\right] + \int C_c(L,t)dx + \frac{P_0(t)-P_L(t)}{\rho} = 0
\end{aligned}
\tag{18}
$$

Replacement of the formal solution for the pressure fields (14) into the beam modal equations (5)-(6), leads to a set of $2N$ nonlinear ODEs, in terms of the modal components $q_n(t)$, $r_n(t)$ and the two unsteady flow rates $Q_1(t)$ and $Q_2(t)$. Together with the two flow rate ODEs (18), they form a closed set of first-order nonlinear differential equations describing the 1D fluid-structure model, in the form

$$
[\mathbf{A}]\{\dot{\mathbf{x}}\} + [\mathbf{B}]\{\mathbf{x}\} = \{\mathbf{C}\} \tag{19}
$$

where $\mathbf{x} = \{r_1(t), \ldots r_N(t), q_1(t), \ldots q_N(t), Q_1(t), Q_2(t)\}$, $[\mathbf{A}]$ and $[\mathbf{B}]$ are (generally dense) matrices of size $2N+2$, and $\{\mathbf{C}\}$ is a vector containing constant flow terms.

Effectively, we are able to discretize our continuous 1D problem into a set of ODEs. However, there are nonlinear terms associated with beam motion (e.g. $\int A_c dx$) which contain modal summations in the denominator. As these terms cannot be simplified analytically, we do not reach "true" time-space separation, in the sense that the formulation does not contain constant spatial operators. These terms need to be calculated at each time-step. Despite this fact, the formulation allows for temporal-integrations of the nonlinear system at very modest computational times.

4 Linear stability analysis

The flow expressions obtained in the previous section can be linearized in order to provide a compact tool for linear stability analysis, which is often the primary concern. To linearize the system of the flow nonlinear equations we firstly separate the governing variables into their steady (zero-order) and fluctuating (first-order) components. Here, we adopt the convention $g(x,t) = \bar{g}(x) + \tilde{g}(x,t)$. Then, by means of a Taylor-series expansion, we linearize the equations by keeping only the zero-order and first-order components. Because under linearized conditions the flow must assume a concrete direction, we will make use of plus-minus $\pm$ and minus-plus $\mp$ signs to distinguish the two scenarios, and avoid duplication of expressions. The uppers signs are used for flow in the positive direction ($P_0 > P_L$) and the lower signs for flow in the negative direction ($P_0 < P_L$).

4.1 Steady equations (zero-order)

The steady components of the velocity (13) and pressure (14) fields are given by

$$\bar{u}_c(x) = \frac{\bar{Q}_c}{\bar{h}_c(x)} \quad ; \quad \bar{p}_c(x) = \rho\frac{1}{2}\left[-\frac{\bar{Q}_c^2}{\bar{h}_c(x)^2} \mp 2\bar{Q}_c^2 f \int\left(\frac{1}{\bar{h}_c(x)^3}\right)dx \right] + \bar{S}_c \tag{20}$$

Assuming a constant driving pressure, i.e. $P_0(t) = P_0$ and $P_L(t) = P_L$, we get, according to (11)-(12), the following steady boundary conditions at $x = 0$ and $x = L$:

$$\bar{p}_c(0) = P_0 - \rho\frac{1}{2}\left(1 \pm K_0\right)\bar{u}_c^2(0) \quad ; \quad \bar{p}_c(L) = P_L - \rho\frac{1}{2}\left(1 \mp K_L\right)\bar{u}_c^2(L) \tag{21}$$

Proceeding in a similar manner as above, we replace the formal solutions (20) into the boundary conditions (21), leading to

$$\bar{S}_c = P_0 \mp \rho\frac{1}{2}\frac{\bar{Q}_c^2}{\bar{h}_c(0)^2}K_0 \quad ; \quad \bar{S}_c = P_L \pm \rho\frac{1}{2}\left(\frac{\bar{Q}_c^2}{\bar{h}_c(L)^2}\right)K_L \pm \rho\bar{Q}_c^2 f\int\left(\frac{1}{\bar{h}_c(L)^3}\right)dx \tag{22}$$

which then gives the expression for the (squared) static flow rate $\bar{Q}_c$ in each channel

$$\bar{Q}_c^2 = \frac{2\left(P_0 - P_L\right)\bar{h}_c^2(0)^2\bar{h}_c^2(L)}{\pm\rho\left[\bar{h}_c^2(0)K_L + \bar{h}_c^2(L)K_0 + 2\bar{h}_c^2(0)\bar{h}_c^2(L)f\int\left(\frac{1}{\bar{h}_c^3(L)}\right)dx\Big|_{x=L}\right]} \tag{23}$$

Replacing the expressions for $\bar{Q}_c$ and $\bar{S}_c$ into (20) will give us expressions for the steady pressure and velocity fields in term of the beam displacement only. Then, the steady pressure difference between the two channels $\Delta\bar{P}(x) = \bar{p}_2(x) - \bar{p}_1(x)$ can be written explicitly. Finally, replacing the expression for the steady pressure difference $\Delta\bar{P}(x)$ into the beam's (static) equations leads to

$$\bar{q}_n = \frac{b\left(P_0 - P_L\right)}{m_n \omega_n^2} \int_0^L \left(\frac{\bar{h}_1^2(0)^2 \bar{h}_1^2(L)\left[\frac{1}{\bar{h}_1^2(x)} \pm \frac{K_0}{\bar{h}_1^2(0)} \pm 2f \int \left(\frac{1}{\bar{h}_1^3(x)} \right) dx \right]}{\pm \left[\bar{h}_1^2(0) K_L + \bar{h}_1^2(L) K_0 + 2\bar{h}_1^2(0)\bar{h}_1^2(L) f \int \left(\frac{1}{\bar{h}_1^3(L)} \right) dx \Big|_{x=L} \right]} - \frac{\bar{h}_2^2(0)^2 \bar{h}_2^2(L)\left[\frac{1}{\bar{h}_2^2(x)} \pm \frac{K_0}{\bar{h}_2^2(0)} \pm 2f \int \left(\frac{1}{\bar{h}_2^3(x)} \right) dx \right]}{\pm \left[\bar{h}_2^2(0) K_L + \bar{h}_2^2(L) K_0 + 2\bar{h}_2^2(0)\bar{h}_2^2(L) f \int \left(\frac{1}{\bar{h}_2^3(L)} \right) dx \Big|_{x=L} \right]} \right) \phi_n(x) dx \quad \text{for } n = 1, 2 \ldots N \tag{24}$$

The final steady problem then becomes a system of N nonlinear algebraic equations whose only variables are the modal displacements $\bar{q}_n$. All other parameters are set: the driving pressure $P_0 - P_L$, the head-loss coefficients K_0, K_L and f, the channel profiles $H_1(x)$ and $H_2(x)$, as well as the beam modal parameters m_n, ζ_n, ω_n and $\phi_n(x)$. This system can be solved numerically, to find the equilibrium beam configurations $\bar{q}_n$. Subsequently, all other steady variables, $\bar{Q}_c$, $\bar{S}_c$, $\bar{u}_c(x)$, $\bar{p}_c(x)$, can be calculated.

4.2 Linearized equations (first-order)

In this section, to avoid duplication of expressions, we present derivations for the upper channel only $(c = 1)$, noting that equivalent expressions can be derived for the lower channel $(c = 2)$. The fluctuating component of the velocity $\tilde{u}_1(x,t)$ is defined as

$$\tilde{u}_1(x,t) = \tilde{Q}_1(t)\bar{F}_{1,n}(x) \pm \sum_{n=1}^{N} \dot{\tilde{q}}_n(t)\bar{A}_{1,n}(x) \pm \bar{Q}_c \sum_{n=1}^{N} \tilde{q}_n(t)\bar{B}_{1,n}(x) \tag{25}$$

and the fluctuating pressure $\tilde{p}_c(x,t)$ is given by

$$\tilde{p}_1(x,t) = \rho \left[\begin{array}{c} \sum_{n=1}^{N} \tilde{q}_n(t) 3\bar{Q}_1^2 \int \bar{C}_{1,n}(x)\,dx - \sum_{n=1}^{N} \dot{\tilde{q}}_n(t) 2\bar{Q}_1 \int \bar{D}_{1,n}(x)\,dx - \sum_{n=1}^{N} \ddot{\tilde{q}}_n(t) \int \bar{A}_{1,n}(x) dx \\ + \tilde{Q}_1(t) 2\bar{Q}_1 \int \bar{E}_1(x)\,dx - \dot{\tilde{Q}}_1(t) \int \bar{F}_1(x) dx \end{array} \right] + \tilde{S}_1(t) \tag{26}$$

where, to simplify notation, the steady auxiliary variables from $\bar{A}_{c,n}(x)$ - $\bar{F}_{c,n}(x)$ are defined as

$$\begin{aligned} &\bar{A}_{c,n}(x) = \frac{\int \phi_n(x) dx}{\bar{h}_c(x)} \quad ; \quad \bar{B}_{c,n}(x) = \frac{\phi_n(x)}{\bar{h}_c{}^2(x)} \quad ; \quad \bar{C}_{c,n}(x) = \frac{\phi_n(x)}{\bar{h}_c(x)^4}\left(\bar{h}_c{}'(x) \mp f \right) - \frac{\phi_n{}'(x)}{3\bar{h}_c{}^3(x)} \; ; \\ &\bar{D}_{c,n}(x) = \frac{\int \phi_n(x) dx}{\bar{h}_c{}^3(x)}\left(\bar{h}_c{}'(x) \mp f \right) - \frac{\phi_n(x)}{\bar{h}_c{}^2(x)} \quad ; \quad \bar{E}_c(x) = \frac{\left(\bar{h}_c{}'(x) \mp f \right)}{\bar{h}_c{}^3(x)} \quad ; \quad \bar{F}_c(x) = \frac{1}{\bar{h}_c(x)} \; ; \end{aligned} \tag{27}$$

To the first order, the boundary conditions at $x = 0$ and $x = L$ become

$$\tilde{p}_c(0,t) = \rho\left(-1 \mp K_0\right)\bar{u}_c(0)\tilde{u}_c(0,t) \; ; \qquad \tilde{p}_c(L,t) = \rho\left(-1 \pm K_L\right)\bar{u}_c(L)\tilde{u}_c(L,t) \; ; \tag{28}$$

Replacing the expressions for the fluctuating velocity (25) and pressure (26) fields into the boundary conditions at $x = 0$, we get

$$\tilde{S}_1(t) = \rho\left(-1 \mp K_0\right)\bar{u}_1(0)\bar{F}_1(0)\tilde{Q}_1(t) \tag{29}$$

and at $x = L$, we get

$$\tilde{S}_1(t) = \rho \begin{bmatrix} \sum_{n=1}^{N} \tilde{q}_n(t)\left[-3\bar{Q}_1^2 \int \bar{C}_{1,n}(L)\,dx - \left(1 \mp K_L\right)\bar{u}_1(L)\bar{Q}_1\bar{B}_{1,n}(L)\right] \\ +\sum_{n=1}^{N} \dot{\tilde{q}}_n(t)\left[-2\bar{Q}_1 \int \bar{D}_{1,n}(L)\,dx - \left(1 \mp K_L\right)\bar{u}_1(L)\bar{A}_{1,n}(L)\right] \\ +\sum_{n=1}^{N} \ddot{\tilde{q}}_n(t)\left[\int \bar{A}_{1,n}(L)dx\right] \\ +\tilde{Q}_1(t)\left[-2\bar{Q}_1 \int \bar{E}_1(L)\,dx - \left(1 \mp K_L\right)\bar{u}_1(L)\bar{F}_{1,n}(L)\right] \\ +\dot{\tilde{Q}}_1(t)\left[\int \bar{F}_1(L)dx\right] \end{bmatrix} \tag{30}$$

Then, combining (29) from (30), we get two linear ODEs (one for each channel) in terms of the fluctuating flow rates $\tilde{Q}_c(t)$

$$\begin{cases} \dot{\tilde{Q}}_1(t)d_1 + \tilde{Q}_1(t)e_1 + \sum_{n=1}^{N} \tilde{q}_n(t)a_{1,n} + \sum_{n=1}^{N} \dot{\tilde{q}}_n(t)b_{1,n} + \sum_{n=1}^{N} \ddot{\tilde{q}}_n(t)c_{1,n} = 0 \\ \dot{\tilde{Q}}_2(t)d_2 + \tilde{Q}_2(t)e_2 - \sum_{n=1}^{N} \tilde{q}_n(t)a_{2,n} - \sum_{n=1}^{N} \dot{\tilde{q}}_n(t)b_{2,n} - \sum_{n=1}^{N} \ddot{\tilde{q}}_n(t)c_{2,n} = 0 \end{cases} \tag{31}$$

where the auxiliary vectors $a_{c,n}$, $b_{c,n}$, $c_{c,n}$ and scalars d_c, e_c, are given by

$$\begin{aligned} a_{c,n} &= -3\bar{Q}_c^2 \int \bar{C}_{c,n}(L)\,dx - \left(1 \mp K_L\right)\bar{u}_c(L)\bar{Q}_c\bar{B}_{c,n}(L) \\ b_{c,n} &= -2\bar{Q}_c \int \bar{D}_{c,n}(L)\,dx - \left(1 \mp K_L\right)\bar{u}_c(L)\bar{A}_{c,n}(L) \\ c_{c,n} &= \int \bar{A}_{c,n}(L)dx \\ d_c &= \int \bar{F}_c(L)dx \\ e_c &= -2\bar{Q}_c \int \bar{E}_c(L)\,dx - \left(1 \mp K_L\right)\bar{u}_c(L)\bar{F}_c(L) + \left(1 \pm K_0\right)\bar{u}_c(0)\bar{F}_c(0) \end{aligned} \tag{32}$$

In order to formulate the fluctuating pressure difference $\Delta\tilde{P}(x,t)$, we need to replace the expression for $\tilde{S}_c(t)$ in the pressure expression (26) of each channel, such that the expression for $\Delta\tilde{P}(x,t)$ becomes dependent solely on the unknown time dependent variables: $\tilde{q}_n(t)$, $\dot{\tilde{q}}_n(t)$, $\ddot{\tilde{q}}_n(t)$, as well as $\tilde{Q}_1(t)$, $\tilde{Q}_2(t)$, $\dot{\tilde{Q}}_1(t)$ and $\dot{\tilde{Q}}_2(t)$. Subsequently, we can project the pressure difference into the beam modal equations. In matrix form, the linearized modal forces $\tilde{F}_m(t)$ are then written as

$$\tilde{F}_m(t) = \begin{pmatrix} \left[\mathrm{M}_{n,m}\right]\left\{\ddot{\tilde{q}}_n(t)\right\} + \left[\mathrm{C}_{n,m}\right]\left\{\dot{\tilde{q}}_n(t)\right\} + \left[\mathrm{K}_{n,m}\right]\left\{\tilde{q}_n(t)\right\} \\ -\left\{\mathrm{R}_{1,m}\right\}\tilde{Q}_1(t) + \left\{\mathrm{R}_{2,m}\right\}\tilde{Q}_2(t) + \left\{\mathrm{T}_{1,m}\right\}\dot{\tilde{Q}}_1(t) - \left\{\mathrm{T}_{2,m}\right\}\dot{\tilde{Q}}_2(t) \end{pmatrix} \quad \text{for } m = 1,2\ldots N \tag{33}$$

where the three matrices, of size $N \times N$, and the four vectors, of size N, are given by

$$
\begin{aligned}
\mathrm{K}_{n,m} &= -3b\rho\int_0^L \left[\bar{Q}_2^2\int \bar{C}_{2,n}(x)\,dx + \bar{Q}_1^2\int \bar{C}_{1,n}(x)\,dx\right]\phi_m(x)dx \;; \\
\mathrm{C}_{n,m} &= -2b\rho\int_0^L \left[\bar{Q}_2\int \bar{D}_{2,n}(x)\,dx + \bar{Q}_1\int \bar{D}_{1,n}(x)\,dx\right]\phi_m(x)dx \;; \\
\mathrm{M}_{n,m} &= b\rho\int_0^L \left[\int \bar{A}_{2,n}(x)dx + \int \bar{A}_{1,n}(x)dx\right]\phi_m(x)dx \;; \\
\mathrm{R}_{c,m} &= b\rho\int_0^L \left[2\bar{Q}_c\int \bar{E}_c(x)\,dx - (1\pm K_0)\bar{u}_c(0)\bar{F}_c(0)\right]\phi_m(x)dx \;; \\
\mathrm{T}_{c,m} &= b\rho\int_0^L \left[\int \bar{F}_c(x)dx\right]\phi_m(x)dx
\end{aligned}
\tag{34}
$$

Finally, letting the (diagonal) mass, damping and stiffness matrices of the (uncoupled) beam be M, C and K, we can build the coupled system by assembling the modal equations together with the two linearized flow ODEs (31). In a first-order formulation, we get

$$
\begin{bmatrix}
([\mathrm{M}_{n,m}]-[M]) & [\mathbf{0}] & \{\mathrm{T}_{1,m}\}^T & -\{\mathrm{T}_{2,m}\}^T \\
[\mathbf{0}] & -[\mathbf{I}] & \{\mathbf{0}\}^T & \{\mathbf{0}\}^T \\
\{c_{1,m}\} & \{\mathbf{0}\} & d_1 & 0 \\
-\{c_{2,m}\} & \{\mathbf{0}\} & 0 & d_2
\end{bmatrix}
\begin{Bmatrix} \dot{\tilde{r}}_n \\ \dot{\tilde{q}}_n \\ \dot{\tilde{Q}}_1 \\ \dot{\tilde{Q}}_2 \end{Bmatrix}
+
\begin{bmatrix}
([\mathrm{C}_{n,m}]-[C]) & ([\mathrm{K}_{n,m}]-[K]) & -\{\mathrm{R}_{1,m}\}^T & \{\mathrm{R}_{2,m}\}^T \\
[\mathbf{I}] & [\mathbf{0}] & \{\mathbf{0}\}^T & \{\mathbf{0}\}^T \\
\{b_{1,m}\} & \{a_{1,m}\} & e_1 & 0 \\
-\{b_{2,m}\} & -\{a_{2,m}\} & 0 & e_2
\end{bmatrix}
\begin{Bmatrix} \tilde{r}_n \\ \tilde{q}_n \\ \tilde{Q}_1 \\ \tilde{Q}_2 \end{Bmatrix} = 0
\tag{35}
$$

This linear system of ODEs, of size $2N+2$, can then be formulated as an eigenvalue problem to infer the stability of the system.

5 Linear stability results and numerical validation

In this section, with the aim of assessing the viability of the 1D simplified modelling approach and validating our results, we compare the linear stability results from our model to reference results. Even though the present modelling approach allows for channels of arbitrary shapes $H_c(x)$, we will consider only symmetric channels of constant section, i.e. $H_1(x) = H_2(x) = H$, on which most literature is based on. For the same reason, we will analyse configurations with flow in the positive direction only.

Following reference studies [2] [12] [17], we will present results in terms of the following non-dimensional parameters

$$
U^* = U_0 L\sqrt{\frac{\rho_s e}{EI}} \quad ; \quad M^* = \frac{\rho_f L}{\rho_s e} \quad ; \quad H^* = \frac{H_0}{L}
\tag{36}
$$

where U^* is a reduced velocity (essentially the inverse of a Strouhal number), M^* is the fluid-beam mass ratio, and H^* is the confinement ratio. In our formulation, $H_0 = H_1(0) + H_2(0)$ and the fluid velocity U_0 is given by the steady component of the inlet velocity, i.e. $U_0 = (\bar{Q}_1 + \bar{Q}_2)/H_0$. Additionally, the Reynolds number Re is accounted implicitly by the Fanning friction coefficient f. To this end, we note the commonly used relation between Reynolds number Re and the friction coefficient f, established based on empirical data of steady flow [31] [32], given by

$$
\begin{cases}
f = 12\,\mathrm{Re}^{-1} & \text{for } \mathrm{Re} < \mathrm{Re}_0 \quad \text{(laminar)} \\
f = 0.055\,\mathrm{Re}^{-0.25} & \text{for } \mathrm{Re} > \mathrm{Re}_0 \quad \text{(turbulent)}
\end{cases}
\tag{37}
$$

where Re_0 is the Reynolds number separating laminar from turbulent flow ranges. Based on these relations, here we have used an analytical approximation presented by Piteau and Antunes [35], which combines the expressions for laminar and turbulent flow, reaching a mixed formulation, applicable in the whole range of Reynolds number, given by

$$f = 12\,\mathrm{Re}^{-1} + 0.055\,\mathrm{Re}^{-1/4} \tag{38}$$

Figure 2 compares the relations (37) with the mixed-flow analytical approximation (38).

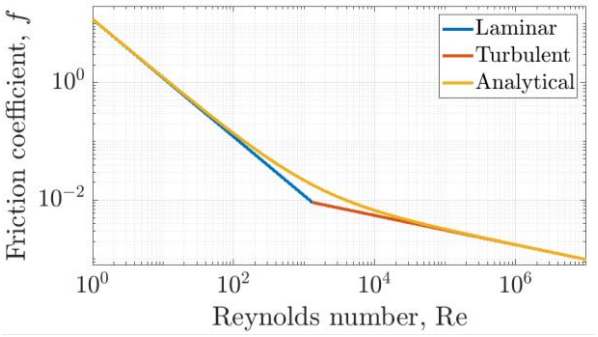

Figure 2 – (color online) Comparison between Hirs friction model (37) with the continuous analytical approximation (38).

5.1 Comparison to results from original 1D leakage-flow model

As a starting point to validate the present formulation, we compare stability results to those published by Nagakura and Kaneko [18], who presented a similar model, with constant and symmetric channel cross-sections. We take the same model parameters used in [18]: the beam has length $L = 200$ mm, width $b = 100$ mm, thickness $e = 0.2$ mm, density $\rho_s = 8780$ kg·m^{-3}, Young's modulus $E = 1.1\times10^{11}$ N·m^2 and modal damping $\zeta = 0.01$; while the fluid has density $\rho_f = 1.2$ kg·m^{-3}, the localised head-loss coefficients are taken as $K_0 = 0$ and $K_L = 1$, and the friction coefficient $f = 0.005$. The channels are symmetric and have a constant section of height $H = 2.5$ mm. This configuration leads to the nondimensional parameters $M^* = 0.136$, $H^* = 1/40$. Figure 3 shows results from the two models, describing the evolution of the eigenvalues s in the complex-plane for varying driving pressure (or fluid inlet velocity U_0). We notice that the stability behaviour of the various coupled modes is described identically by the two models, asserting the viability of the proposed resolution.

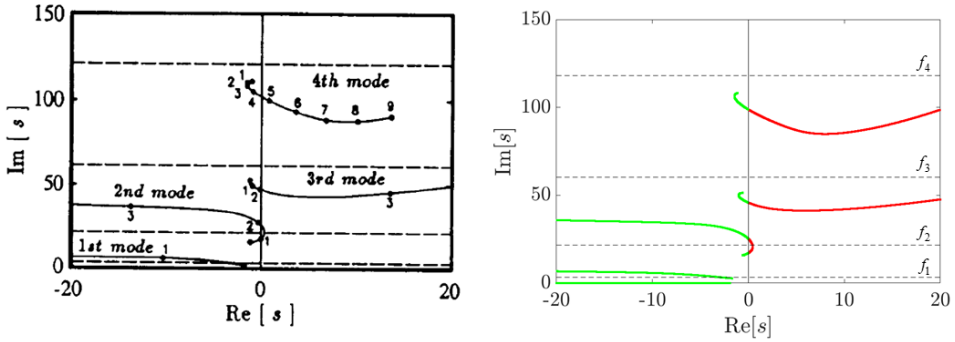

Figure 3 – (color online) Evolution of the eigenvalues of the coupled structure-fluid system as a function of driving pressure, shown in the complex-plane. Results from the present model are shown on the right while the analogous presented in [18] are on the left. The dotted lines correspond to the frequencies f_n of the in-vacuo beam modes. Note that, following [18], the eigenvalues are normalized by the constant $\sqrt{EI/mL^4}$, where m is the total mass of the beam. In the right plot, green and red lines represent stable and unstable eigenvalues.

5.2 Comparison to results from a 2-D viscous model

To evaluate the potential of the proposed simplified modelling approach, we now compare linear stability results to those obtained from models with more involved physics, which are assumed to provide a more realistic representation of the system dynamics. Namely, we will refer to the results presented by Cisonni et al. [17], which have used a viscous 2D model to calculate various stability maps as a function of the non-dimensional parameters U^*, M^*, H^* and Re. In their paper [17], a 2D model is used to solve the nonlinear Navier-Stokes equations in the time-domain, including viscous effects. Several parametric sweeps were carried out to obtain stability curves in the nondimensional (U^*M^*) plane, for several (H^*, Re) pairings. For each parametric configuration, simulations were run for at least 10 periods of oscillations, from which stability conditions and corresponding frequencies were extracted.

As a first example, Figure 4 shows a typical stability map in the (U^*M^*) plane, calculated with the present model and with the 2-D viscous model. Here, an undamped beam was considered, $\zeta_n = 0$, the confinement ratio was set at $H^* = 1/10$ and the Reynolds number at $\mathrm{Re} = 100$. Note that, in our formulation, the Reynolds number is set implicitly following relation (38), which leads to a friction coefficient $f \approx 0.14$. On the left are the stability boundaries in the (U^*M^*) plane and on the right the frequencies of the corresponding neutrally stable modes.

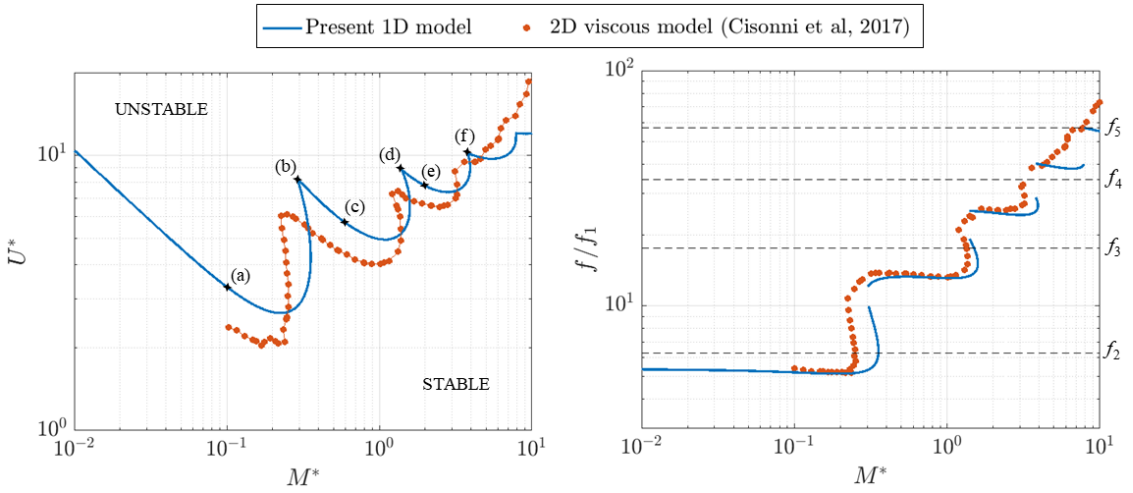

Figure 4 – (color online) Stability boundary in the (U^*M^*) plane (left) and the corresponding frequencies (right) for a system with confinement $H^* = 1/10$ and Reynolds number $\mathrm{Re} = 100$. The 2-D model results were retrieved from those presented in [17].

The cascading stability boundary shown in Figure 4 is a typical result of cantilevered structures subject to axial flow, reported in many previous studies, including models which assume inviscid flow (see review in [2]). We note that results from the present model agree qualitatively well with those from the 2D model. Despite some minor quantitative differences, the overall stability behaviour of the system is well encapsulated. Namely, the sharp transitions in the stability curves, associated with the well-known mode-switching behaviour and illustrated clearly by the abrupt changes in the instability frequency, are well represented. This behaviour occurs at increasing mass-ratios, whereby the first unstable mode in the system transitions from lower to higher order, i.e. the main unstable (coupled) mode is dominated by (in-vacuo) beam modes of progressively higher order. To clarify, Figure 5 illustrates the complex mode shapes associated with the various points (a)-(f) indicated in Figure 4. The minor quantitative differences (slight vertical and horizontal shifts in the $M^* - U^*$ plane), are likely explained by the inherent differences in the 1D and 2D modelling approaches, namely, the explicit vs. implicit account of viscous effects or the parabolic vs. constant velocity profiles stemming from explicit/implicit account of boundary layer effects.

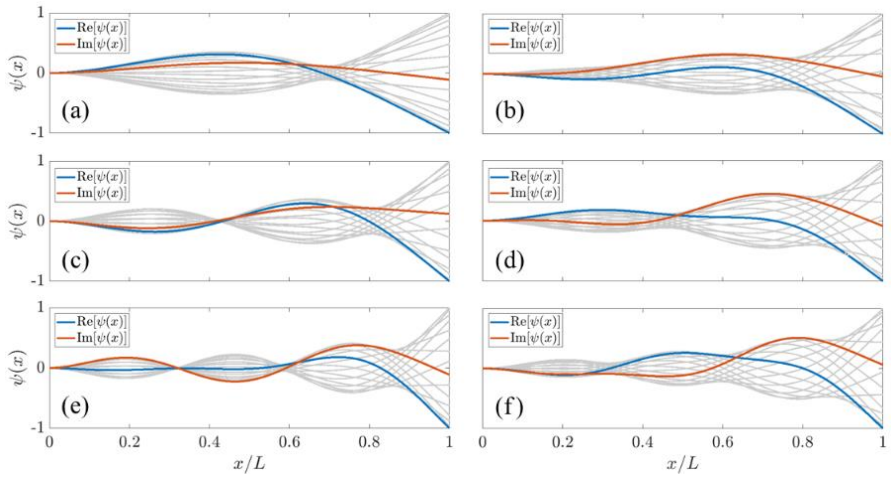

Figure 5 – (color online) Complex mode-shapes of the neutrally-stable modes associated with the boundary points (a)-(f) indicated in Figure 4. The real and imaginary parts of the mode shapes are indicated in blue and red, respectively. The grey lines illustrate the actual beam motion associated with the corresponding complex mode shapes.

5.3 The effect of confinement

Again, following the results from Cisonni et al, we investigate the effects of the confinement. In Figure 6 we show stability boundaries in the (U^*, M^*) plane for systems with different confinement ratios $H^* = [1/4,\ 1/8,\ 1/10]$. Results from our 1D model are shown on the left and results from the 2D viscous model of Cisonni et al. on the right.

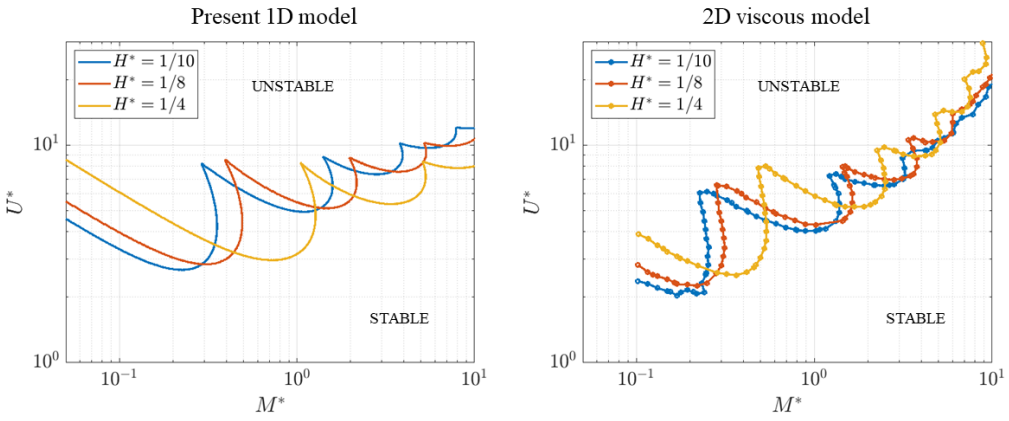

Figure 6 – (color online) Stability boundary in the (U^*, M^*) plane, for an undamped beam with different confinement ratios. The results from our model are shown on the left plot, while the results from Cisonni et al. at the right. The Reynolds number was fixed at $\mathrm{Re} = 100$ (in the present model, this implies $f = 0.14$).

The two sets of stability boundaries shown in Figure 6 shows us that the 1D model is able to correctly predict the effects of the confinement, as the behavioural trends are well characterised, namely that larger confinements H^*: (1) tend to stabilise de system, particularly for light beams (small M^*); and (2) push the mode-switching behaviour towards larger mass-ratios. However, we underline that, quantitatively, results start to deviate from those of the 2D model for larger confinement ratios. Notice that, at $H^* = 1/4$, the first modal-transition occurs at approximately $M^* = 0.5$ for the 2D model and at approximately $M^* = 1$ for the 1D model. These deviations are not unexpected since the 1-D bulk-flow equations are derived on the assumption that channel heights are small compared with the characteristic length of the system. Therefore, we expect deviations to increase for larger confinement ratios H^*. These deviations are likely explained by the fact that no explicit account of circulatory flow effects appears in the simplified 1-

D bulk-flow formulation. While circulatory flow will likely have a minor influence on the flutter instability in narrower confinements, this will not be true for wider confinements. In the limiting case of a beam in unbounded flow, the derived bulk-flow modelling approach is clearly not suitable. We also note that, on all three cases, the stability for heavier beams $\left(M^* > 5\right)$ is underestimated, with the 2D model predicting the first instabilities at larger velocities. Regarding lower confinement ratios, the lack of results from the 2D model for confinement ratios $H^* < 1/10$ prevents us from a concrete comparison. However, based on the trends of the results shown above, it is expected that the 1D model will provide accurate representations at smaller confinements.

6 Time-domain integrations and nonlinear dynamics

In this section we aim to explore the nature of the nonlinear regimes associated with a linearly unstable system through numerical time-domain integration. The set of nonlinear ODEs described in Section 3 was solved using MATLAB's solver `ode15i` [36], an implicit scheme with variable time-stepping, which allowed fast computations by alternating between long and short time-step to account for the naturally stiff impact dynamics. Numerical simulations were started with the solutions of the steady configuration $\bar{q}_n$, $\bar{Q}_c$ as initial conditions, and a small perturbation force was applied to all beam modes to induce eventually unstable dynamics.

6.1 Stability and impact boundaries

As a first step to characterise the nonlinear behaviour of the system, we examine the role of impacts and when they are more likely to occur. For this, a series of numerical time-domain integrations were performed in the non-dimensional parametric space (U^*, M^*). We considered a symmetric configuration with confinement ratio $H^* = 1/10$, and friction coefficient $f = 0.14$. The simulations were run for several seconds until one of the following scenarios was encountered: (1) oscillations gradually decreased converging to the steady solution (linearly stable dynamics), (2) the oscillations grew until a stable limit cycle was reached, without the occurrence of impacts, or (3) oscillations grew until the beam eventually comes into contact with one of the walls, at which point the simulations were stopped. The difference between the latter two scenarios enabled us to estimate an "impact boundary", that is, a frontier in the (U^*, M^*) plane separating limit cycles with and without impacts. Because contact was not accounted in this first study, the beam was described by only $N = 10$ modes. All modal damping coefficients were set to $\zeta_n = 0.01$. The resulting map is shown in Figure 7.

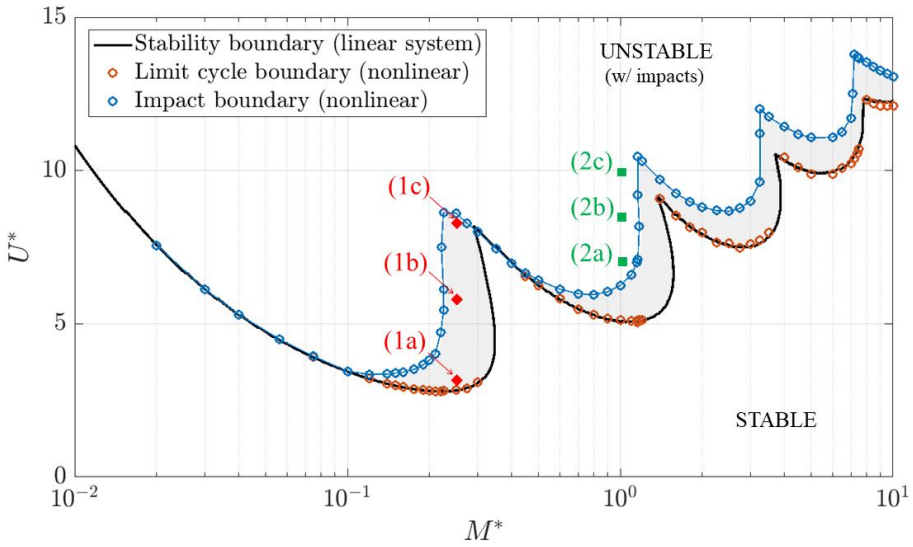

Figure 7 – (color online) Stability map of a system with confinement ratio $H^* = 1/10$ and friction coefficient $f = 0.14$, in the (U^*, M^*) plane. The linear stability boundary (black line) is compared to the limit cycle boundary found by the nonlinear simulations (orange dots). The impact boundary (blue line) illustrates the frontier in which unstable dynamics lead to contact between the beam and the confinement walls. The nonlinear limit cycles associated with the points marked (1a-c) and (2a-c) will be shown in the following sections.

Firstly, we see that the stability boundary predicted by the linearized system is coherent with the unstable dynamics observed in the nonlinear simulations. As for the impact boundary, we note that the regions in which limit cycles without impacts occur (grey area) are not extensive. Noticeably, we underline the fact that for small mass ratios (heavy beams or light fluids) these regions simply do not exist and the flutter instability, however weak, inevitably leads to large amplitude beam motions and eventual contact with the side walls. This seems physically plausible as the inertia of heavier beams will tend to outweigh the restoring forces from a light fluid.

At this point is it important to mention that experimental studies on similar systems (with bounded or unbounded flow) often report hysteretic behaviour, suggesting the existence of a subcritical bifurcation [8] [37] [38]. That is: (1) when the mean flow velocity is gradually increased, an initially static beam will start fluttering at a specific critical velocity U_c, and on the other hand, (2) when the mean flow velocity is gradually decreased, an initially unstable (fluttering) beam will stabilise at a different critical velocity U_d. This phenomenon remains to this day an open question and modelling efforts generally fail to reproduce this behavior. Some authors [37] [38] have suggested that the fluttering instability of cantilever plates/beams could actually be supercritical (no hysteresis) and that the hysteresis found in experiments could be a product of unaccounted three-dimensional effects, i.e. edge-vortices, torsional motion of the plate, etc. Some preliminary numerical studies have been conducted using the current model and no hysteresis was found yet. Nevertheless, we believe the present approach could be used in the future as a framework for bifurcation studies (using algorithms for the continuation of periodic solutions), which would give a more comprehensive view of the nonlinear dynamics of the model, and perhaps clarify some of these unanswered questions.

6.2 Elastic impact model

The few researchers who explored nonlinear simulations of cantilevered plates in confined axial flow, eventually encounter limitations in their solutions, at regimes where the motion of the plate is large enough that collisions with the walls become inevitable. Nevertheless, numerous experimental (and modelling) observations [7] [8] [26] [24] [39] demonstrate that nonlinear motions regularly present intermittent impacts, particularly for cases where the confinement and/or the mass ratio are low.

At this point it is worth discussing the nonlinear behavior of the flow in the eminence of a channel constriction. Firstly, it must be said that, for systems composed of fluttering cantilever beams, channel constriction (or collapse) will generally occur at the beam tip. As one might expect, a local constriction of the channel initially leads to an increase of the local velocity and a decrease in local pressure, further pushing the beam towards the wall. However, this behavior is eventually limited by the effect of the nonlinear flow dissipation terms (frictional effects as well as head-losses at the trailing edge). Moreover, as the beam motion becomes very large, its inertia in the direction of a channel wall will cause a "squeeze" like effect on the fluid. In the eminence of contact, because the fluid is assumed incompressible, this "squeezing" effect will lead to an abrupt, but continuous, decrease in local velocity (and even locally reverse flow), at which point, if fluid forces are not strong enough to oppose the beam inertia, contact becomes inevitable. Naturally, this phenomenon will be more pronounced in configurations with low mass ratios. Additionally, we note that compressibility effects, such as propagating pressure waves, are not accounted in our model, and we do not discard the possibility that, in particular scenarios, such effects could have a meaningful impact on the dynamics of a real physical system.

As mentioned in the introduction, the addition of dynamic impacts to the fluid-structure model is a non-trivial task. Not only do we need to formulate the contact conditions between the beam and the side walls, which often implies dynamic constraints (at the displacement, velocity and acceleration levels), but also the associated contact conditions for the flow. The latter difficulty relates to the fact that the solutions for flow velocity and pressure fields present singularities at the moment of contact, i.e. when the channel height $h_c = 0$. Moreover, classical penalty methods, reliant on contact interpenetration, are naturally incompatible with the flow model. In this paper, we do not aim to find solutions to these delicate issues. However, we present a pragmatic approach based on a regularized impact formulation, in the spirit of classical penalty methods, that allows us to include impacts in a simple manner that is compatible with the flow formulation.

Since the fluid equations do not allow for beam penetration on the wall, the impact force is applied on the beam just before contact. That is, an impact force $F_i(x,t)$ is applied in regions of the beam which have trespassed a small regularization parameter ε, as illustrated in Figure 8. In essence, we allow some flow leakage at the moments of "contact", such that an impact force can applied to the beam without fully restricting the flow dynamics.

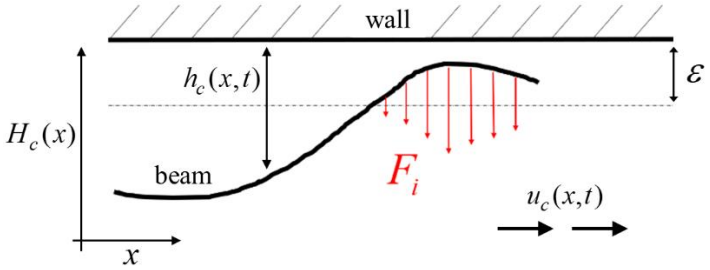

Figure 8 – Illustration of the beam violation right before contact and corresponding impact force.

The simplest and most commonly used approaches to describe dynamic impacts between two solids are based on the Hertz model, a purely elastic contact model (without dissipation), typically in the form

$$F_i(x,t) = \begin{cases} k_i\, v^p(x,t) & \text{if } v(x,t) > 0 \\ 0 & \text{otherwise} \end{cases} \tag{39}$$

where k_i is an impact stiffness, $p > 1$, and the violation amplitude is given, in our case, by $v(x,t) = \varepsilon - h_c(x,t)$. The sign of $F_i(x,t)$ is defined for each channel: $F_i > 0$ for $c = 2$; $F_i < 0$ for $c = 1$. These models describe a nonlinear stiffening force proportional to a power p of the violation amplitude. For purely mechanical problems, these types of models are well behaved. However, in our problem, the inertial forces of the beam and the fluid forces might, in some cases, dominate over the contrary impact force, and penetration occurs nonetheless, i.e. $h(x,t) < 0$. For this reason, we have pragmatically used an infinitely stiffening impact force in the form

$$F_i(x,t)=\begin{cases} k_i \tan\left[\dfrac{v(x,t)}{\varepsilon}\left(\dfrac{\pi}{2}\right)\right] & \text{if } \; h_c(x,t)<\varepsilon \\ 0 & \text{otherwise} \end{cases} \tag{40}$$

where, in this case, penetration is avoided completely as the impact force tends to infinity when $h_c(x,t)\to 0$. Figure 9 compares the amplitude of the impact force for various values of impact stiffness k_i with the linear case (Eq. (39) with $p=1$), as a function of the normalized amplitude of violation v/ε.

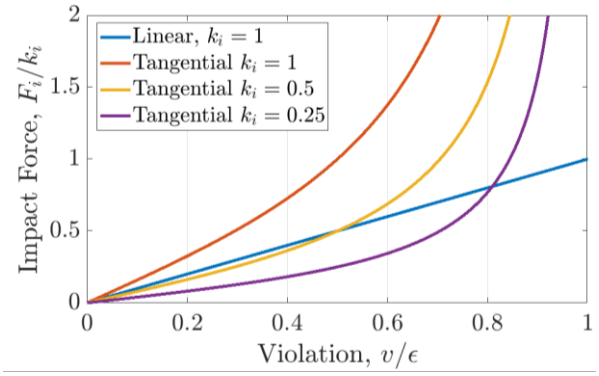

Figure 9 – (color online) Impact force as a function of the amplitude of violation (when $h<\varepsilon$). A linear stiffness impact model is compared to the tangential impact model for various values of stiffness k_i.

6.3 Limit cycles without impacts

To illustrate the character of the limit cycles we start by showing the solutions to a set of configurations that lead to stable limit cycles without impacts. The configurations (1a), (1b) and (1c) - red points in Figure 7 – have a constant mass ratio $M^*=0.25$ and various reduced velocities $U^*=[3.5,\ 6,\ 8]$, respectively. For each configuration (1a), (1b) and (1c), Figure 10 shows snapshots of the beam motion and Figure 11 shows the temporal evolution of the modal velocities $r_n(t)$ and the unsteady flow rates $Q_c(t)$. Additionally, in Figure 12 we show the phase-portrait of the beam tip, the evolution of the tip displacement $y(L,t)$, the spectra of the tip velocity and average contribution of each (in-vacuo) beam modes to the nonlinear oscillations, expressed by the root-mean-square (RMS) value of modal displacements $q_n(t)$.

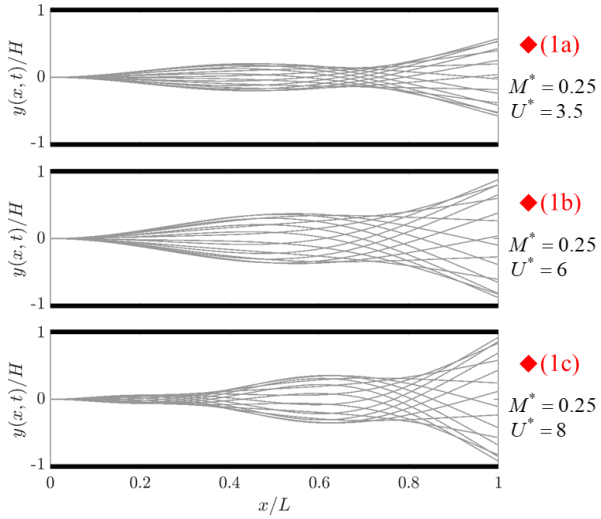

Figure 10 – (color online) Snapshots of the beam motion during one cycle for configurations (1a), (1b) and (1c).

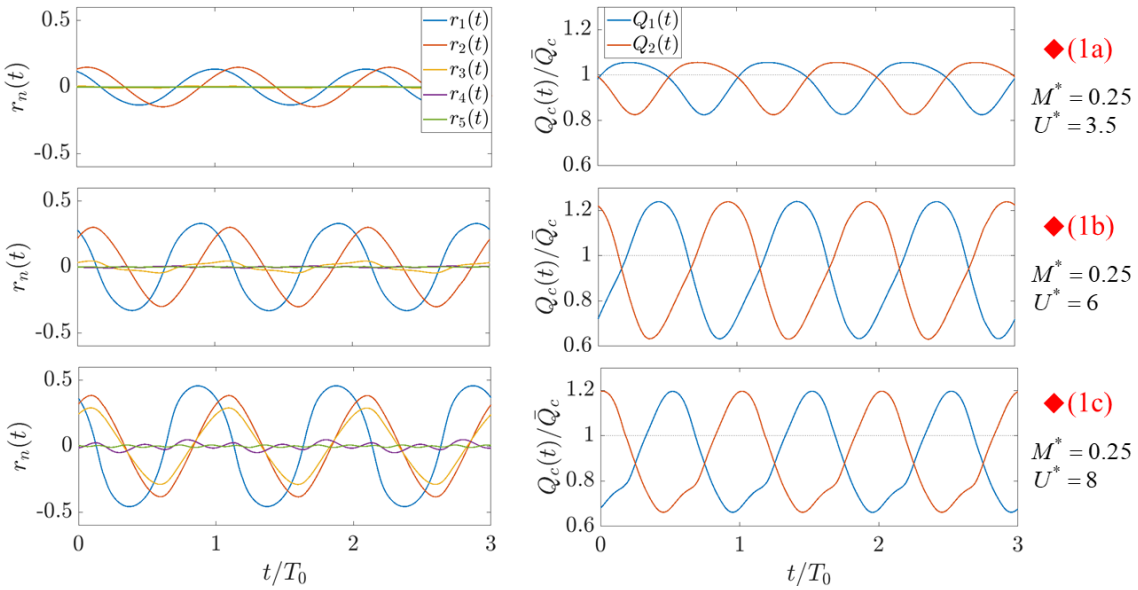

Figure 11 – (color online) Temporal evolution of the modal velocities $r_n(t)$ (left) and unsteady flow rates $Q_c(t)$ (right) in the limit cycles associated with configurations (1a), (1b) and (1c). For clarity, time scales are normalized by the fundamental period of the corresponding limit-cycle T_0.

Figure 10 shows that the amplitude of the beam motion tends to increase with increasing velocity U^*, as expected. Moreover, we notice that the beam motion also changes qualitatively. At lower velocities (1a) the motion is dominated by the first two in-vacuo beam modes, while at larger velocities (1b-c) the contribution of the third beam mode becomes increasingly significant, illustrating a "mode-transition", similar to what was observed in the linear stability results. Moreover, the beam motions in the various limit cycles are remarkably similar to the complex mode shapes presented in Figure 5, suggesting that, in these cases, the overall motion of the fluttering beam is not altered significantly by the nonlinear fluid forces.

In Figure 11, the modal velocities again show the appearance of the third beam mode at larger velocities (1c). We also note a growing nonlinearity with increasing velocities U^* (1b-c), as the oscillations of the modal components start to drift from the nearly sinusoidal motions seen in (1a). As expected from a symmetric system, the flow rates $Q_c(t)$ oscillate in phase opposition. Moreover, they oscillate around a value slightly lower than their steady component $\bar{Q}_c$. This means that the overall mass transport is reduced by the fluttering beam, compared to a static scenario. This seems physically plausible as, during flutter, some of the energy carried by the flow is transferred to the beam and lost through either structural dissipation or increased flow-dissipation effects (either friction along the domain or turbulent effects in the trailing edge, modelled by the distributed and localized head-loss terms, respectively).

The plots in Figure 12 suggest that, without intermittent impacts, the nonlinearity in the beam motion is relatively weak. Naturally, the shown spectra contain only odd harmonics, as would be expected from a symmetric system. At lower velocities (1a), the motion is nearly sinusoidal, with negligible contributions from higher harmonic components while at larger velocities U^*, higher-order harmonic components become more significant, however, still relatively weak compared to the fundamental frequency (amplitudes of higher harmonics are typically 20/30 dB below the fundamental).

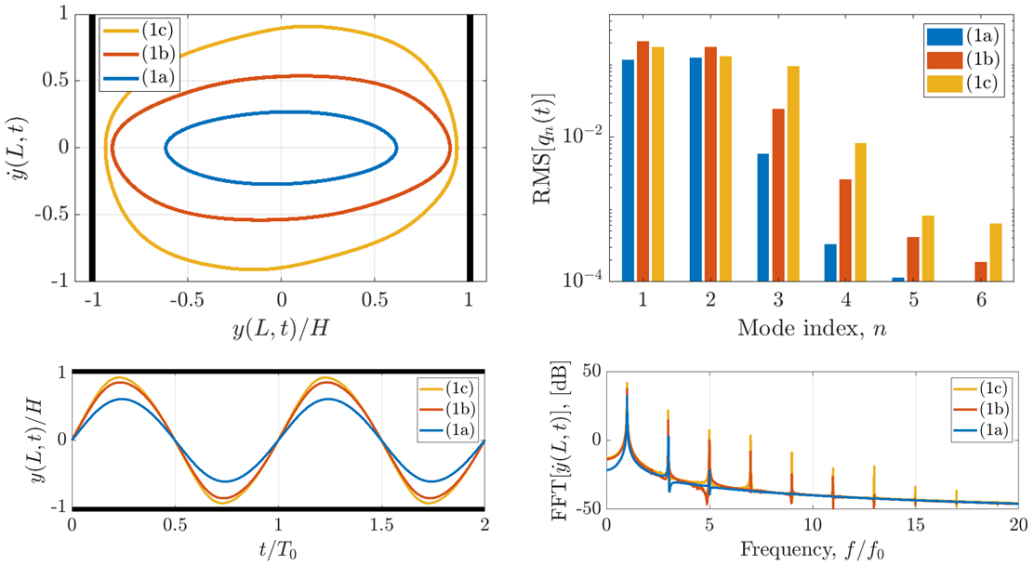

Figure 12 – (color online) Phase-portrait of beam tip (top-left); Root-mean-square (RMS) value of the modal displacements (top-right); beam tip displacement (bottom-left) and spectra of the tip velocity (bottom-right), for the three configurations (1a), (1b) and (1c). For clarity, time/frequency scales are normalized by the fundamental period/frequency of the corresponding limit cycle T_0 and f_0.

6.4 Limit cycles with impacts

Here we illustrate a few limit cycles that include intermittent impacts, namely, the solutions for the configurations indicated in Figure 7 by points (2a), (2b) and (2c). These configurations have a constant mass ratio of $M^* = 1$ and various reduced velocities $U^* = [7,\ 8.5,\ 10]$, respectively. For these simulations, a large number of beam modes was considered, $N = 40$, to ensure the impact dynamics are well represented. In general, the number of considered modes N should be such that the modal stiffness of the highest considered mode is somewhat larger than the impact stiffness at the point of contact x_i, that is $k_i < m_N \omega_N^2$. The effect of the impact stiffness, k_i, deserves a meaningful discussion, as it might affect the resulting limit cycles. However, we will firstly show some illustrative results and, in a following section, we will discuss the role of the impact stiffness and how it affects the resulting nonlinear behaviour. In the following simulations, the non-dimensional impact stiffness was taken as $k_i^* = k_i / m_1 \omega_1^2 = 10^7$ (normalized by the stiffness of the first beam mode) and the non-dimensional regularization parameter $\varepsilon/H = 10^{-3}$.

Figure 13 shows snapshots of the beam motion and Figure 14 the evolution of the modal velocities $r_n(t)$ and the unsteady flow rates $Q_c(t)$, for the three configurations (2a), (2b) and (2c). In Figure 15 we show the phase-portrait of the beam tip, the evolution of the tip displacement $y(L,t)$, the spectra of the tip velocity and RMS-value of the modal displacements $q_n(t)$, for all three configurations. Moreover, we show in Figure 16 the impact force applied on the beam throughout the limit cycles. The impact force is expressed as the spatial integral of $F_i(x,t)$, normalized by a reference force $F_0 = m f_1^2 H$, where m is the total mass of the beam and f_1 is the frequency of the first in-vacuo beam mode.

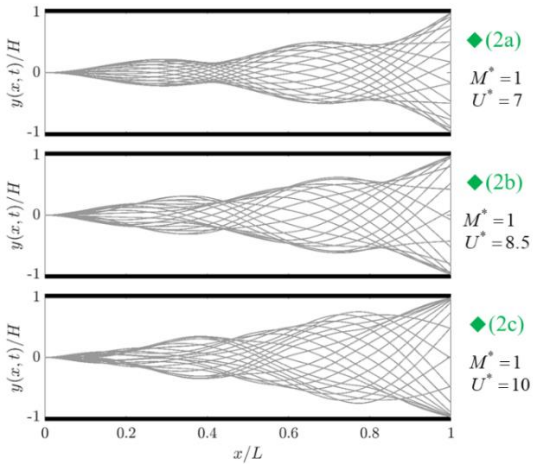

Figure 13 - (color online) Snapshots of the beam motion during one cycle for configurations (2a), (2b) and (2c).

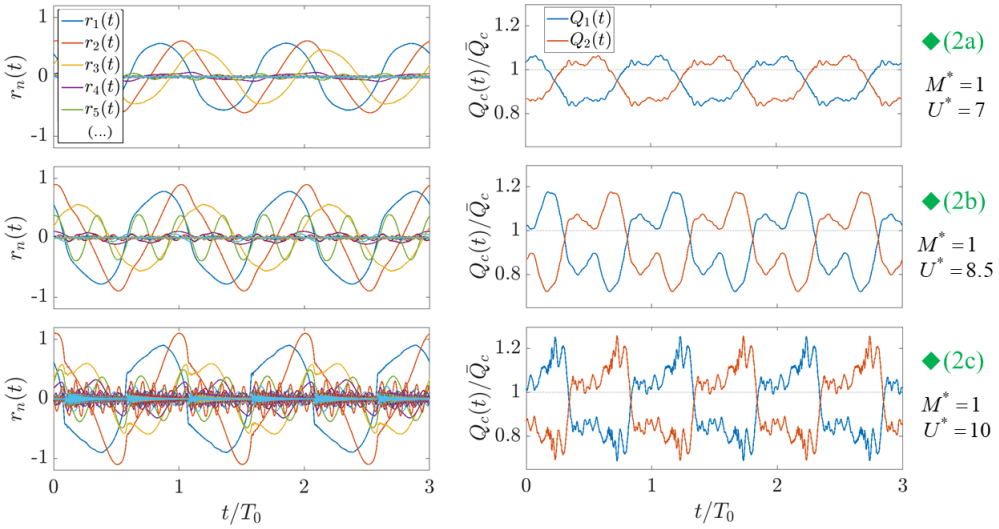

Figure 14 - (color online) Temporal evolution of the modal velocities $r_n(t)$ (left) and unsteady flow rates $Q_c(t)$ (right) in the limit cycles associated with configurations (2a), (2b) and (2c). For clarity, time scales are normalized by the fundamental period of the corresponding limit-cycle T_0 .

In Figure 13 we notice that, in all cases, intermittent contact occurs solely at the tip of the beam. As the velocity U^* increases (2b-c), impacts become more violent and the beam motion becomes increasingly perturbed, as higher order beam modes are intermittently excited and start playing a more prominent role in the overall beam motion. These effects are also seen by the evolution of the modal velocities shown in Figure 14 and the RMS-values in Figure 15 . When impacts are relatively weak (2a), the tip simply "grazes" the wall and the overall beam motion is not significantly altered compared to the mode shapes estimated by the linear stability analysis.

Similarly, the oscillations of the flow rates become increasingly abrupt in the presence of violent impacts. However, it is interesting to note that sharp changes in the unsteady flow-rate (e.g. bottom-right plot in Figure 14) do not occur at the moments of contact but rather at the moments when the beam motion rapidly shifts from one side of the channel to the other. This effect can be illustrated, for example, by the beam-tip motion shown in Figure 15. Here we notice that as impacts become stronger, the overall contact time also becomes larger, meaning as well that the beam-tip will shift sides more abruptly, hence generating sharp fluctuations in the flow-rates.

In Figure 15 we note that the motions become increasingly nonlinear in the presence of stronger impacts. The phase-portrait shows more perturbed motions with larger gradients. Naturally, the spectra of the beam tip show a large number of high order harmonic components, increasing in amplitude as impacts become

more violent. It is worth noting that, in limit cycles with stronger impacts (2c), the oscillations are not strictly periodic. Although the low frequency motions are stable, we notice small high frequency perturbations, related to the unsynchronized motion of the intermittently excited higher order beam modes. This behaviour is clearly illustrated by the spectra of (2c), where we notice not only an increase in the amplitude of the harmonics, but also a visible presence of noise-like spectral behaviour. Nevertheless, these motions might be tentatively classified as perturbed periodic oscillations, rather than aperiodic dynamics.

For illustrative purposes, the time and frequency scales were normalized by the fundamental period/frequency of each limit cycle. However, it is worth noting that larger reduced velocities U^* led to limit cycles with higher fundamental frequency f_0. For reference, the fundamental frequencies f_0 of the limit cycles (2b) and (2c) were 11% and 23% larger than the fundamental frequency of the (2a) limit cycle, respectively. This is not unexpected since larger velocities U^*, as well as impacts, will provide additional stiffness to the unstable FSI mode.

The impact forces represented in Figure 16 illustrate the fact that, during each beam-wall interaction, the beam tip impacts the wall multiple times. This chattering effect is a typical behaviour of systems with impacts in multi-modal structures. In weaker impacts (2a) we notice only a few impacts of decreasing strength while in more violent regimes (2b-c) contact is composed of multiple impacts with stronger associated forces and an overall longer chattering time.

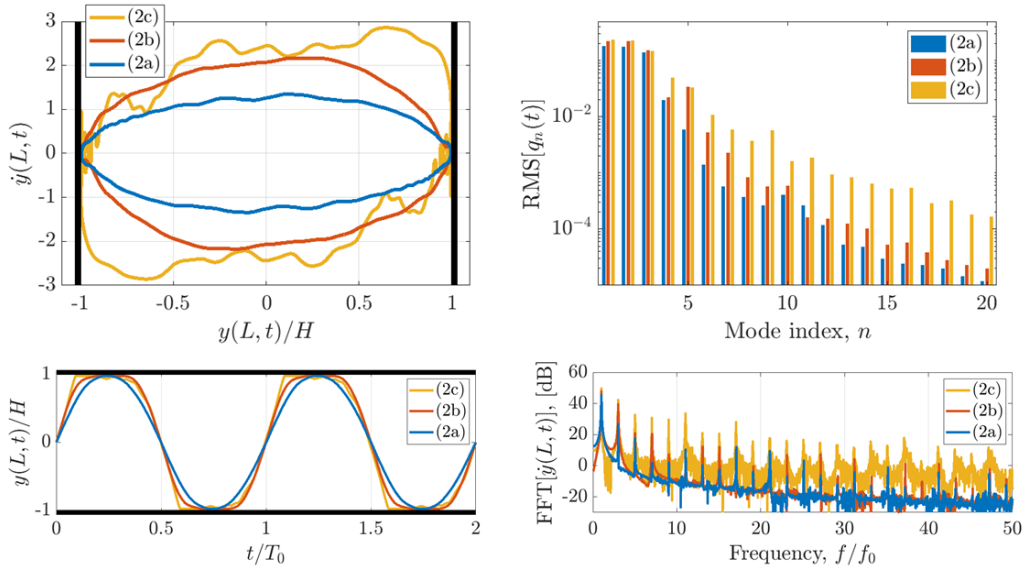

Figure 15 - (color online) Phase-portrait of beam tip (top-left); root-mean-square (RMS) value of the modal displacements (top-right); beam tip displacement (bottom-left) and spectra of the tip velocity (bottom-right, for the three configurations (2a), (2b) and (2c). For clarity, time/frequency scales are normalized by the fundamental period/frequency of the corresponding limit-cycle T_0 and f_0.

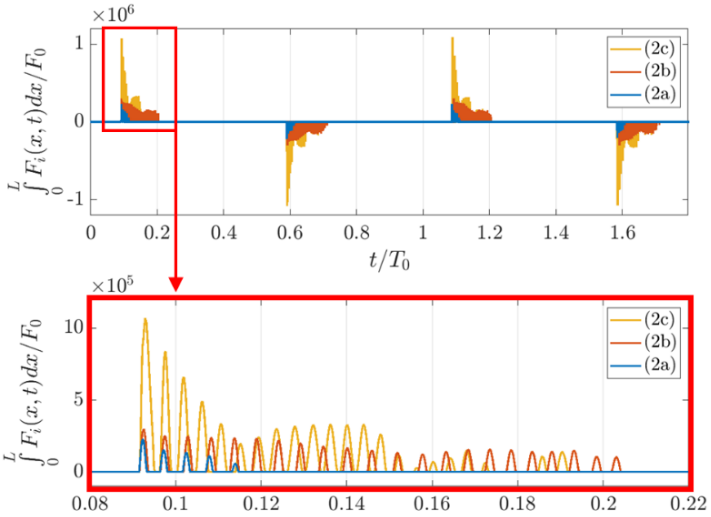

Figure 16 – (color online) The evolution of the non-dimensional impact force through the limit-cycles associated with configurations (2a), (2b) and (2c). For clarity, time scales are normalized by the fundamental period of the corresponding limit cycle T_0.

6.5 Limit cycles in asymmetric configurations

To contrast with the symmetric limit cycles shown above, we now considered a similar system where the lower channel height is taken as $H_2 = 2H_1$. The mass ratio is fixed at $M^* = 1$, as in (2a-c), and two reduced velocities are considered $U^* = [7,\ 9]$. The following examples illustrate the diversity of behaviour found in asymmetric system, leading to limit cycles with either one and two impacts per cycle. Figure 17 shows snapshot of the beam motion during the two asymmetric limit cycles. In Figure 18, we see the temporal evolution of modal velocities and flow rates. Figure 19 shows the phase portrait of the beam tip, the evolution of the tip displacement and the spectra of the tip velocity in the two asymmetric configurations.

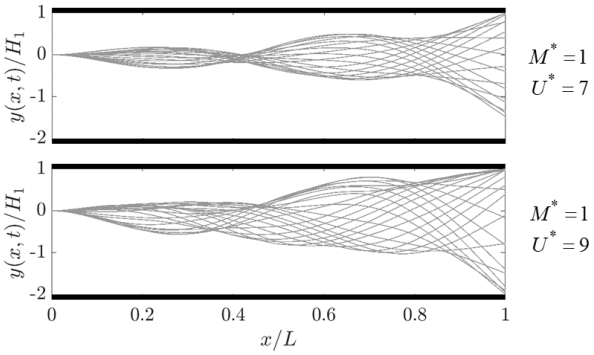

Figure 17 – Snapshot of the beam motion in limit cycles with impacts in asymmetric configurations.

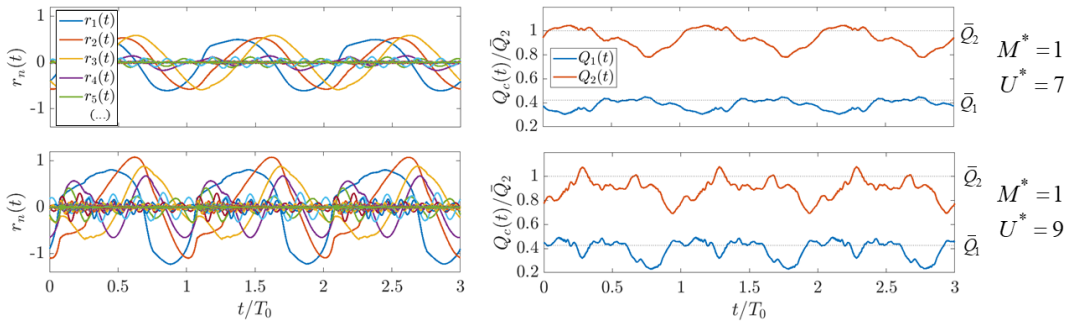

Figure 18 – (color online) Temporal evolution of the modal velocities (left) and unsteady flow rates (right) in the two asymmetric configurations. For clarity, time scales are normalized by the fundamental period of the corresponding limit-cycle T_0.

Once again, in the examples shown in Figure 17-Figure 19, impacts occur solely at the tip of the beam. In the $(M^* = 1\ ; U^* = 7)$ configuration, impacts occur only at the upper wall (one per cycle) while in the $(M^* = 1\ ; U^* = 9)$ configuration there are two impacts per cycle, on both the upper and lower walls. The latter case presents more violent impacts and a more distorted beam motion, which includes significant contributions from higher order beam modes. The spectra in Figure 19 now shows both even and odd harmonic, as expected from an asymmetric system.

As expected in asymmetric cases, the overall flow rates are larger in the wider channel, as fluid velocities tend to equalize under the same driving pressures. Nonetheless, static flow velocities on the narrower channel $\bar{u}_1$ will actually be lower than in the wider channel $\bar{u}_2$ due to increased flow-dissipation. Consequently, the beam will feel larger perturbation pressures from the upper channel, which will push the overall beam motion towards the lower channel, as seen clearly in Figure 17.

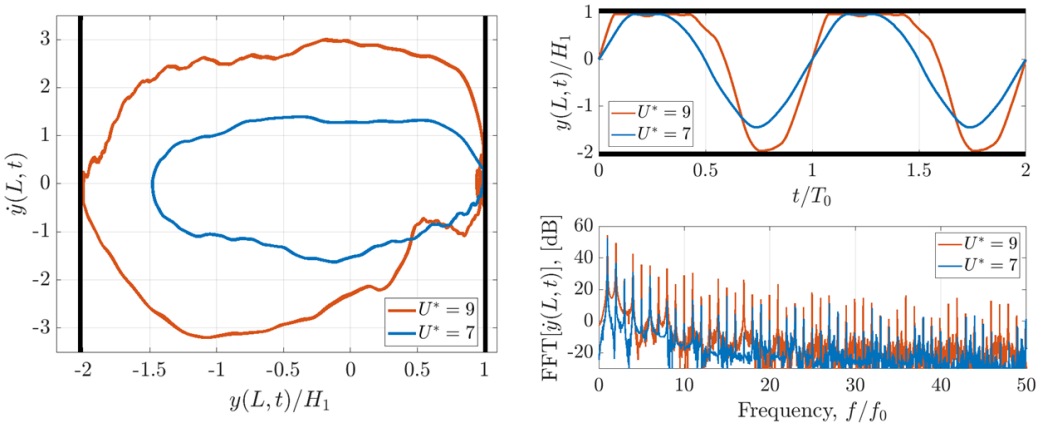

Figure 19 – (color online) Phase-portrait of the beam tip (left); beam tip displacement (top-right) and spectra of the beam tip velocity (bottom-right) for the two asymmetric configurations. For clarity, time/frequency scales are normalized by the fundamental period/frequency of the corresponding limit-cycle T_0 and f_0.

6.6 Limit cycles with impacts at multiple locations

Now we illustrate a limit cycle where, contrary to the previous, impacts occur not only at the tip of the beam. We consider an asymmetric configuration with $H_2 = 4H_1$, $M^* = 1$ and $U^* = 12$, with all other parameters as before. Figure 20 illustrates the character of the resulting limit cycle.

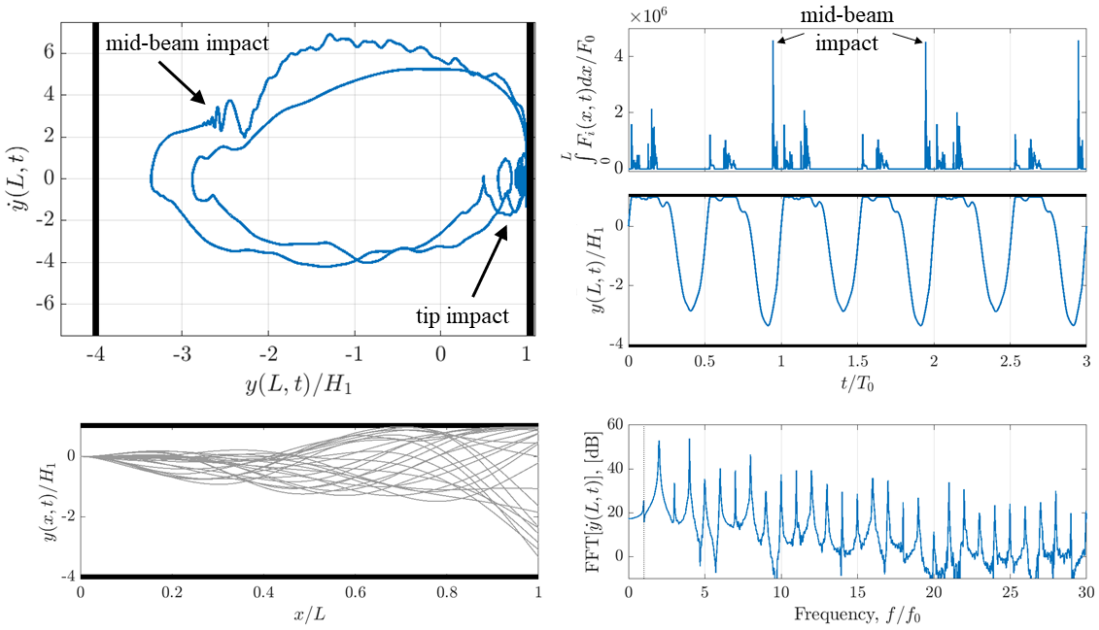

Figure 20 – (color online) Illustration of a limit cycle with impacts both at the tip and along the beam. Phase-portrait of the beam tip (top-left); temporal evolution of the impact force (top-right) and the tip displacement (centre-right); snapshots of the beam motion (bottom-left) and the spectra of the beam tip velocity (bottom-right). For clarity, time/frequency scales are normalized by the fundamental period/frequency of the limit cycle T_0 and f_0.

The results in Figure 20 are qualitatively different from those previously presented. The snapshots of the beam motion illustrate how the beam impacts the walls both at the tip and also along the beam $(x/L \approx 0.7)$. In the phase-portrait of the tip motion, we notice that, throughout one cycle, the beam impacts the upper wall three times, once in a mid-beam location and twice at the beam tip.

Curiously, the spectra shows that the first harmonic component is much weaker than the second one. Furthermore, the oscillations of the tip displacement and the phase-portrait show the same effect in the temporal domain, as the "principal" motion nearly repeats itself within one cycle. These results suggest that, in this case, the mid-beam impact might induce some form of period-doubling bifurcation.

6.7 Aperiodic dynamics

So far, we have only examined periodic limit cycles at relatively low/moderate reduced velocities U^*. However, at larger reduced velocities, strong fluid forces and violent impacts may lead to aperiodic/chaotic dynamics. To illustrate, we now consider a symmetric system, similar to those described in Section 7.3, with a mass ratio $M^* = 0.05$ and reduced velocity $U^* = 25$. Figure 21 illustrates the aperiodicity of the fluid-structure dynamics.

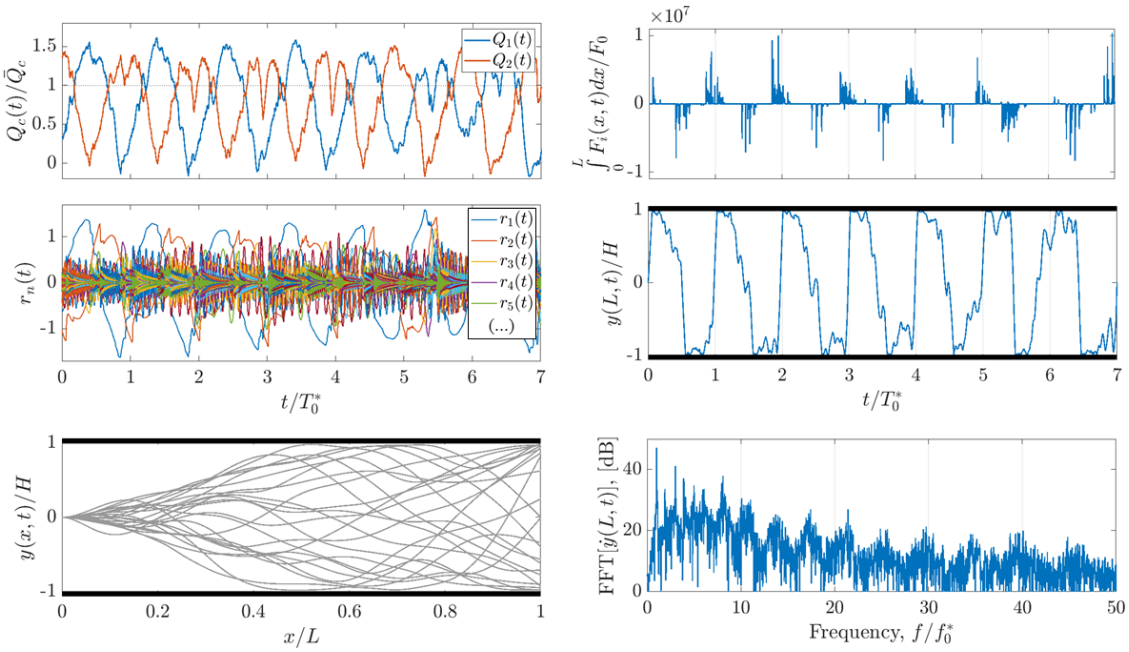

Figure 21 - (color online) Illustration of aperiodic dynamics in a symmetric system with $M^* = 0.05$ and $U^* = 25$. Temporal evolution of the flow rates (top-left), the nondimensional impact forces (top-right), the modal velocities (centre-left) and the tip displacement (centre-right); snapshots of the beam motion (bottom-left) and the spectra of the beam tip velocity (bottom-right). Time and frequency scales are normalized by a pseudo-fundamental period/frequency, T_0^* and f_0^*.

Notice that, despite the clear aperiodicity of the motion, there is some form of regularity in the low frequency behaviour (see prominence of a low frequency component in the spectra shown in Figure 21). For this reason, time and frequency scales are normalized by a pseudo-fundamental period/frequency, T_0^* and f_0^*, given by the low frequency component with largest magnitude.

Contrary to the previously shown periodic behaviour, here impacts occur in diverse locations along the beam, in the region $0.3 < x/L < 1$. The violent impacts at different locations strongly excite higher order beam modes, in an irregular manner. Despite this, the oscillations of the first two beam mode contributions seem have some form of regularity (see evolution of modal velocities). This relatively stable motion is more clearly illustrated by the spectra of the tip velocity, which, despite its wide-band nature, also shows the prominence of some frequencies in the low frequency range. In the previous shown example (2c), we discussed the presence of small (high frequency) perturbations to the limit cycles. The present dynamics might be seen from the perspective that these perturbations cease to have a negligible effect, and now, clearly break periodicity.

6.8 The effect of impact stiffness

Finally, to assess the role of the impact stiffness on the resulting nonlinear behaviour, we now take one example configuration and show the resulting limit cycles calculated with different impact stiffnesses k_i. The configuration was symmetric, as above, with $H^* = 1/10$, $M^* = 0.1$ and $U^* = 8$. A total of 40 beam modes were considered, with uniform modal damping $\zeta_n = 0.01$. The impact regularization parameter was fixed at $\varepsilon/H = 10^{-3}$, and the non-dimensional impact stiffness $k_i^* = k_i / m_1 \omega_1^2$, was varied from 10^5 to 10^8. Figure 22 shows the phase-portrait of the beam tip, the tip displacement and the spectra of the tip velocity for the limit cycles with various values of impact stiffness k_i. Additionally, Figure 23 shows the impact forces applied on the beam (integrated in space) for the various limit cycles.

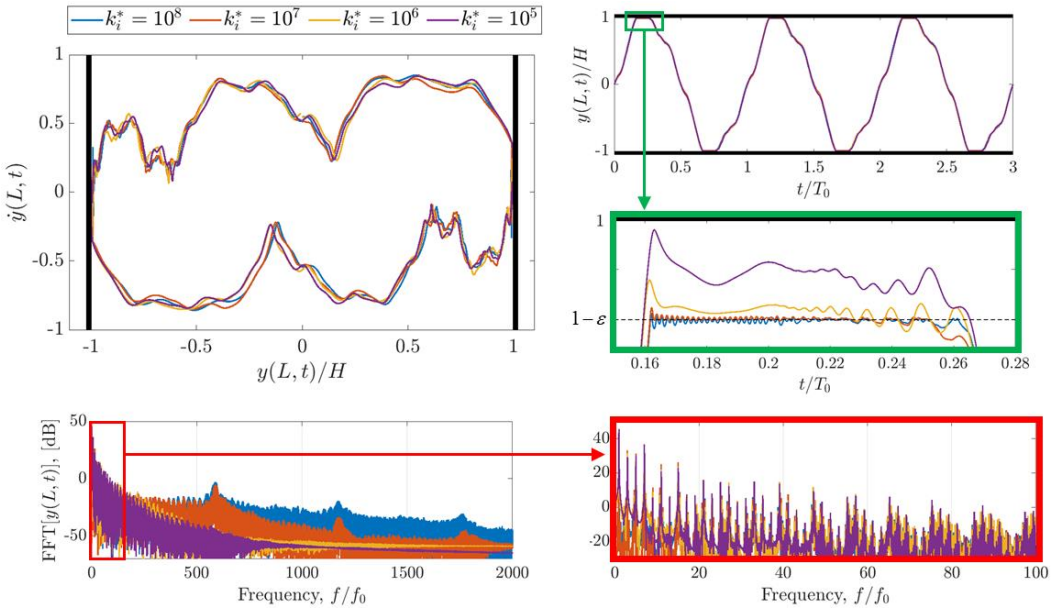

Figure 22 – (color online) Comparison of limit cycles with intermittent impacts, calculated with various impact stiffnesses. The phase-portrait of the beam tip (top-left); the beam tip displacement (top-right); and the spectra of the beam tip velocity (bottom). For clarity, time/frequency scales are normalized by the fundamental period/frequency of the corresponding limit-cycle T_0 and f_0.

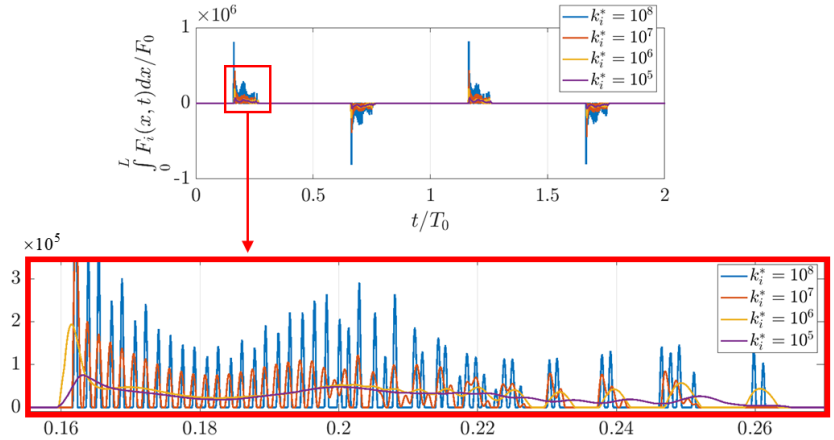

Figure 23 – (color online) The evolution of the non-dimensional impact force (integrated in space) through the limit-cycles for using various values of impact stiffness. For clarity, time scales are normalized by the fundamental period of the corresponding limit-cycle T_0.

The results above show us that the impact stiffness does not seem to affect the overall motion of the limit cycle. The phase-portrait of the beam tip shows only minor quantitative differences. From the evolution of the beam tip displacement during the impact, we notice that a larger impact stiffness results in very small "penetration" and a chattering of higher frequency. As the impact stiffness if softened, penetration becomes more pronounced and the chattering effects are smoothened. Despite this, the overall contact time remains fairly regular in all 4 cases. These effects are clearly illustrated by the frequency content of the tip motion. We notice that low frequency components remain nearly unchanged and noticeable differences are seen only at the high-frequencies. This example suggests that, using the current impact model, the choice of impact stiffness brings only minor quantitative changes but does not alter the overall dynamics of the system, at least in the tested range of impact stiffnesses. Many other configurations were tested (not shown here), leading to similar conclusions. However, the possibility of qualitative changes due to varying impact stiffness is not discarded and further studies are necessary.

7 Conclusions

In this paper we have presented a framework for the comprehensive study of the nonlinear dynamics of a flexible beam subject to axial flow in a confined passage. Previous studies have been constrained by either large computational costs associated with 2D CFD models, the lack of a nonlinear flow formulation, and/or more importantly, by the occurrence of contact between the beam and the side-walls. Here, a 1D model was formulated where the beam is described by its in-vacuo modes and incompressible bulk-flow equations, including distributed and localised head-losses, are used for the flow in both channels. An analytical resolution, based on the formal solutions for the velocity and pressure fields, is developed and leads to a fully nonlinear formulation of the fluid-structure interaction. Moreover, the possibility of contact between the beam and the walls is accounted for by a regularized impact model.

As a preliminary assessment of the potential of the proposed approach, results of linear stability analysis were compared to reference results using more realistic 2D CFD models. Overall, results were positively validated over a wide range of the non-dimensional parameters (mass ratio and reduced velocity), with only minor quantitative differences, at least for relatively narrow passages. At larger confinement ratios H/L, we notice larger errors, as expected from the simplifying assumptions made in the bulk-flow approach.

Subsequently, a variety of nonlinear time-domain integrations were performed in order to illustrate the diversity of dynamical behaviour occurring in such systems. Firstly, several simulations were performed to characterise the nonlinear dynamics for different configurations in the (M^*, U^*)-space. This led to a mapping of the nonlinear dynamics, separating the regions where limit cycles with and without impacts occur. Results suggest that, for low mass ratios (heavy beams/light fluids), the initial flutter instability always leads to contact, likely due to the contrast of the inertia of a heavy beam to that of a light fluid. For moderate-to-large mass ratios, there are regions in the (M^*, U^*)-space where limit cycles without impacts occur, although these are relatively narrow.

Finally, several illustrative simulations are shown including limit cycles (1) with and without intermittent impacts, (2) in symmetric and asymmetric configurations, and (3) with impacts at the beam tip or along its length. Additionally, we show an example where large flow velocities lead to aperiodic/chaotic dynamics. The lack of experimental data on the ensuing limit cycles prevents us from a meaningful validation of our results, nevertheless, they seem physically plausible and consistent with reported experimental observations, at least qualitative.

To the authors best knowledge, the presented framework allowed, for the first time, the calculations of the post-instability behaviour of fluttering beams in confined flow, including vibro-impact dynamics. Future work might deal with the refinement of the impact model, to treat flow contact conditions and include damping. Moreover, bifurcation analysis using methods for the calculation and continuation of periodic solutions can contribute to a more comprehensive understanding of the associated nonlinear dynamics.

8 Acknowledgments

The authors gratefully acknowledge the financial support given by “Fundação para a Ciência e Tecnologia” (FCT – Portugal) through the PhD grant referenced SFRH/BD/140598/2018.

9 References

[1] P. Hidalgo, S. Jha and A. Glezer, "Enhanced heat transfer in air cooled heat sinks using aeroelastically fluttering reeds," *Thermal Investigations of ICs and Systems (THERMINIC),* pp. 1-6, 2015.

[2] K. Shoele and R. Mittal, "Flutter instability of a thin flexible plate in a channel," *Journal of Fluid Mechanics,* vol. 786, pp. 29-46, 2016.

[3] S. Sherrit, H. Lee, P. Walkemeyer, T. Winn, L. Tosi and T. Colonius, "Fluid flow nozzle energy harvesters," *Sensors and Smart Structures Technologies for Civil, Mechanical, and Aerospace Systems,* vol. 9435, 2015.

[4] L. Tosi, "Fluid-Structure Instability in an Internal Flow Energy Harvester (Ph.D. Thesis)," California Institute of Technology, 2018.

[5] F. Avanzini and M. Walstijn, "Modelling the mechanical response of the reed-mouthpiece-lip system of a clarinet. Part 1: a one-dimensional distributed model," *Acta Acustica United with Acustica,* vol. 90, pp. 537-547, 2004.

[6] M. Walstijn and F. Avanzini, "Modelling the Mechanical Response of the Reed-mouthpiece-lip System of a Clarinet. Part II: A Lumped Model Approximation," *Acta Acustica united with Acustica,* vol. 93, pp. 435-446, 2007.

[7] L. Huang, "Mechanical Modeling of Palatal Snoring," *Journal of the Acoustical Society of America,* vol. 97, pp. 3642-3648, 1995.

[8] Y. Aurégan and C. Depollier, "Snoring: Linear Stability Analysis and In-Vitro Experiments," *Journal of Sound and Vibration,* vol. 188, no. 1, pp. 39-54, 1995.

[9] M. P. Paidoussis, Fluid-Structure Interactions: Slender Structures and Axial Flow, San Diego, California: Academic Press, 2004.

[10] S. Kaneko, T. Nakamura, F. Inada and M. Kato, Flow-Induced Vibrations: Classifications and Lessons from Practical Experiences, Amsterdam, Netherlands: Elsevier, 2008.

[11] A. Kornecki, E. Dowell and J. O'Brien, "On the aeroelastic instability of two-dimensional panels in uniform imcompressible flow," *Journal of Sound and Vibration,* vol. 47, no. 2, pp. 163-178, 1976.

[12] C. Guo and M. Paidoussis, "Stability of rectangular plates with free-edges in two-dimensional inviscid channel flow," *Journal of Applied Mechanics ,* vol. 67, pp. 171-176, 2000.

[13] L. Huang, "Flutter of cantilevered plates in axial flow," *Journal of Fluids and Structures,* vol. 9, pp. 127-147, 1995.

[14] Y. Tanida, "Stability of a soft plate in channel flow (aerodynamic aspects of palatal flutter)," *JSME International Journal,* vol. 44, pp. 8-13, 2001.

[15] G. Tetlow and A. Lucey, "Motions of a cantilevered flexible plate in viscous channel flow driven by a constant pressure drop," *Communications in Numerical Methods in Engineering,* vol. 25, no. 5, pp. 463-482, 2009.

[16] L. P. Tosi and T. Colonious, "Modelling and simulation of a fluttering cantilever in channel flow," *Journal of Fluids and Structures,* vol. 89, pp. 174-190, 2019.

[17] J. Cisonni, A. Lucey, N. Elliot and M. Heil, “The stability of a flexible cantilever in viscous channel flow,” *Journal of Sound and Vibration,* vol. 396, no. 26, pp. 186-202, 2017.

[18] H. Nagakura and S. Kaneko, “Stability of a cantiliver beam subject to one-dimensional leakage flow,” *Proceedings Asia-Pacific Conference '93, Kitakyushiu, Japan,* vol. 1, pp. 352-359, 1993.

[19] F. Inada and S. Hayama, “A Study on the Leakage-Flow-Induced Vibrations. Part 1: Fluid Dynamic Forces and Moments Acting on the Walls of a Narrow Tapered Passage,” *Journal of Fluids and Structures,* vol. 4, pp. 395-412, 1990.

[20] F. Inada and S. Hayama, “A Study on the Leakage-Flow-Induced Vibrations. Part 2: Stability Analysis and Experiments for Two-Degree-of-Freedom Systems Combining Translational and Rotational Motions,” *Journal of Fluids and Structures,* vol. 4, pp. 413-428, 1990.

[21] S. Taneda, “Waving Motions of Flags,” *Journal of the Physical Society of Japan,* vol. 24, no. 2, pp. 392-401, 1968.

[22] D. Tang, H. Yamamoto and E. Dowell, “Flutter and limit cycle oscillations of two-dimensional panels in three-dimensional axial flow,” *Journal of Fluids and Structures,* vol. 17, pp. 225-242, 2003.

[23] Y. Yadykin, V. Tenetov and D. Levin, “The flow induced vibration of a flexible strip hanging vertically in parallel flow. Part 1: temporal aeroelastic instability,” *Journal of Fluids and Structures,* vol. 15, pp. 1167-1185, 2001.

[24] S. Alben, “Flag flutter in inviscid channel flow,” *Physics of Fluids,* vol. 27, no. 033603, 2015.

[25] X. Wu and S. Kaneko, “Linear and Nonlinear analyses of sheet flutter induced by leakage flow,” *Journal of Fluids and Structures,* vol. 20, pp. 927-948, 2005.

[26] K. Fujita, H. Morikazu and A. Shintani, “A consideration on pre- and post-instability of an axisymmetric elastic beam subject to axil leakage flow,” *Journal of Fluids and Structures,* vol. 23, pp. 463-478, 2007.

[27] T. Balint and A. Lucey, “Instability of a cantilevered flexible plate in viscous channel flow,” *Journal of Fluids and Structures,* vol. 20, pp. 893-912, 2005.

[28] C. Touzé and O. Thomas, “Reduced-order modelling for a cantilever beam subjected to harmonic forcing,” in *EUROMECH 457,* Fréjus, France, 2004.

[29] J. Antunes and P. Piteau, “A nonlinear analytical model for the squeeze-film dynamics of parallel plates subject to axial flow,” *Journal of Fluids and Structures,* vol. 52, pp. 1491-1504, 2010.

[30] G. Hirs, “A bulk-flow theory for turbulence in lubricant films,” *ASME Journal of Lubrication Technology,* vol. 95, pp. 137-146, 1973.

[31] R. Blevins, Fluid Dynamics, New York, USA: Van Nostrand Reinhold Company, 1984.

[32] I. Idel'Cik, Handbook of Hydraulic Resistance, Boca Raton, USA: CRC Press, 1994.

[33] P. Piteau and J. Antunes, “A theoretical model and experiments on the nonlinear dynamics of parallel plates subject to laminar/turbulent squeeze-film forces,” *Journal of Fluids and Structures,* vol. 33, pp. 1-18, 2012.

[34] S. Kaneko and H. Nagakura, “The stability of a cantilever beam subjected to one-dimensional leakage flow,” *Transactions of the Japan Society of Mechanical Engineers Series C,* vol. 91, pp. 36-43, 1992.

[35] P. Piteau and J. Antunes, “A theoretical model and experiments on the nonlinear dynamics of parallel plates subjected to laminar/turbulent squeeze-film forces,” *Journal of Fluids and Structures,* vol. 33, pp. 1-18, 2012.

[36] “MATLAB - Numerical Integration and Differential Equations,” Mathworks, Inc., 2021. [Online]. Available: https://www.mathworks.com/help/matlab/ref/ode15i.html.

[37] C. Eloy, R. Lagrange, C. Souilliez and L. Schouveiler, “Aeroelastic instability of cantilevered flexible plates in uniform flow,” *Journal of Fluid Mechanics,* vol. 611, pp. 97-106, 2008.

[38] L. Tang and M. Paidoussis, “On the instability and the post-critical behaviour of two-dimensional cantilevered flexible plates in axial flow,” *Journal of Sound and Vibration,* vol. 305, pp. 97-115, 2007.

[39] X. Wu and S. Kaneko, “Linear and nonlinear analyses of sheet flutter induced by leakage flow,” *Journal of Fluids and Structures,* vol. 20, pp. 927-948, 2005.